Synthesis and characterization of triangulene

Niko Pavliček[1]*, Anish Mistry[2]*, Zsolt Majzik[1], Nikolaj Moll[1], Gerhard Meyer[1], David J. Fox[2], Leo Gross[1]

1. IBM Research–Zurich, 8803 Rüschlikon, Switzerland
2. Department of Chemistry, University of Warwick, Gibbet Hill Road, Coventry, CV4 7AL, UK

** These authors contributed equally to this work*

Triangulene, the smallest triplet ground state polybenzenoid (also known as Clar's hydrocarbon), has been an enigmatic molecule ever since its existence was first hypothesized[1]. Despite containing an even number of carbons (22, in 6 fused benzene rings), it is not possible to draw Kekulé-style resonant structures for the whole molecule: any attempt results in two unpaired valence electrons[2]. Synthesis and characterization of unsubstituted triangulene has not been achieved because of its extreme reactivity[1], although the addition of substituents has allowed the stabilization and synthesis of the triangulene core[3, 4] and verification of the triplet ground state via electron paramagnetic resonance measurements[5]. Here we show the on-surface generation of unsubstituted triangulene consisting of six fused benzene rings. The tip of a combined scanning tunnelling and atomic force microscope (STM/AFM) was used to dehydrogenate precursor molecules. STM measurements in combination with density functional theory (DFT) calculations confirmed that triangulene keeps its free molecule properties on the surface, whereas AFM measurements resolved its planar, threefold symmetric, molecular structure. The unique topology of such non-Kekulé hydrocarbons results in an open-shell π-conjugated graphene fragments[6] which give rise to high-spin ground states potentially useful in organic spintronic devices[7, 8]. Our generation method renders manifold experiments possible to investigate triangulene and related open-shell fragments at the single-molecule level.

Figure 1 illustrates the generation of triangulene from a mixture of dihydrodibenzo[*cd,mn*]pyrene isomers (**2**, also denoted as dihydrotriangulenes) as precursor molecules. Compound **2** was deposited on Cu(111), NaCl(100), and Xe(111) surfaces to generate triangulene (**1**) by means of atomic manipulation. STM/AFM is an ideal combination to study on-surface synthesis ranging from individual molecules[9, 10] to graphene nanoribbons[11, 12]. The chemical structure of reactants and products can be resolved by means of AFM with functionalized tips[13]. Even molecules too elusive to be studied by other means[14, 15] can be stabilized by using an ultrathin insulating film as a decoupling

layer. A decoupling layer also facilitates studying the frontier molecular orbitals of the free molecule by means of STM and scanning tunnelling spectroscopy (STS)[16].

Figure 2 presents STM and AFM images of four different molecular species of compound **2** adsorbed on NaCl. As expected, different isomers of dihydrotriangulene are observed. This observation can be discussed by a comparison of Fig. 2e and Fig. 2f, showing the non-equivalent isomers **2a** and **2b** which we found on the surface, respectively. Because the former isomer is prochiral with respect to adsorption, we also observed its surface enantiomer (see Supplementary Fig. 5). Note that **2a** is about three times more abundant than the highly symmetric **2b**, although two Clar sextets can be drawn for both species. This difference can be rationalized by the resonance energy of its aromatic benzo[*c*]phenanthrene core, which is slightly greater than the sum of the resonance energies of the anthracene and benzene cores for **2b** isomers[2]. Furthermore, the resonance energy of an aromatic pyrene core for structures **2c** or **2d** (not observed in the experiment) is appreciably lower. These considerations are consistent with similar observations for benzo[*cd*]pyrenes[17] and are also confirmed by DFT calculations favouring **2a** by 21 meV over **2b**, but by 207 meV over **2c** isomers (see Supplementary Table 1). Thus, we anticipate that we measured an ensemble of molecules representative of compound **2**. We also observed oxidized species comprising a ketone group (Figs. 2g, h) in addition to the dihydro-isomers. A ketone group can be identified by its dark (more attractive) appearance in the AFM images as known from studies on 6-oxo-6H-benzo[*cd*]pyrene[17, 18]. Remarkably, the ketone **3** in Fig. 2g represents an oxidized structure of **2** that was already reported by Clar and Stewart[1]. A comparison of STM and AFM data reveals that in the STM images a tiny sharp kink arises at the position of a single CH_2 group. In contrast, a ketone group leads to a fainter bulge in STM images (Figs. 2c, d) and a lower contrast of the hexagon involved. The central carbon of the three adjacent CH_2 group in **3** adopts the expected tetrahedral bond angle for sp^3 carbon leading to sharp ridges in both STM and AFM mode (Figs. 2c, g) because of strong tilting of the CO molecule at the tip apex.

We dehydrogenated promising candidates (**2a** and **2b** molecules) to obtain triangulene by means of atomic manipulation[14, 15, 19]. To this end, we first positioned the tip above a molecule. Then, we opened the feedback loop and retracted the tip by 0.5 to 0.7 nm to limit the tunnelling current to a few picoamperes. Finally, we increased the voltage to values ranging from 3.5 to 4.1 V for several seconds. In many cases, this procedure also resulted in a lateral displacement of the molecule. When a subsequent STM image indicated a change in the appearance of the molecule, we recorded AFM

images to obtain its structure. Using this procedure, we did not observe any changes in the molecular structure other than the removal of single hydrogens from a CH_2 groups throughout our experiments. The C-H bonds within CH_2 groups act as predetermined breaking points because their bond dissociation energy (3.4 eV in 9,10-dihydroanthracene[20]) is lower than that of corresponding bonds in CH groups (4.8 eV in benzene[21]). This atomic manipulation procedure, exemplified by STM and AFM images shown in Supplementary Fig. 9, proved successful on all investigated surfaces, and was applied twice to an individual dihydrotriangulene (**2**) to generate triangulene (**1**). In some cases, a single voltage pulse induced dissociation of both hydrogens.

Triangulene (**1**), retaining D_{3h} symmetry, does not match the square lattice of (100)-oriented NaCl surfaces[22]. Although triangulene can be generated on NaCl, the symmetry mismatch leads to frequent rotations between four equivalent adsorption geometries (see Supplementary Fig. 8). For this reason, we carried out in-depth characterizations of triangulene on Xe(111) and Cu(111) surfaces sharing its C_3 rotational symmetry. An AFM image of triangulene adsorbed on Cu (Fig. 3a) confirms the expected C_3 symmetry of the molecular structure. The AFM data unambiguously demonstrates stable adsorption without any signatures of chemical bonding to the supporting Cu surface. Instead, the brighter appearance (less attractive) of the peripheral carbons suggests a slightly bent adsorption with the outer carbons further away from the surface, as observed previously for pentacene on Cu(111)[18]. This observation is in strong contrast to previously investigated diradicals that form strong covalent bonds when adsorbed on copper under the same conditions[14, 15], and can be rationalized by the fact that these comprise σ radicals, whereas triangulene features π radicals. Finally, Fig. 3b shows a similar AFM image of a triangulene molecule adsorbed on Xe. In this case, the frequency shift data shows less pronounced differences between inner and outer carbons corroborating a planar molecular structure.

To scrutinize triangulene's peculiar electronic structure, we performed STS and STM orbital imaging on Xe[16]. While a thorough investigation of the spin ground state and excited states is certainly of great interest, we emphasize that this is beyond the scope of this paper. Here, we restrict ourselves to a study of triangulene's frontier molecular orbitals and a comparison to theory.

At this point, before we delve into the experimental results, we present results of spin-polarized DFT calculations of free triangulene. First, our calculations favour the (ferromagnetic) triplet state over the (nonmagnetic) closed-shell and (antiferromagnetic) open-shell singlet state by 0.35 eV and 0.16

eV in energy, respectively. While DFT is appropriate to calculate ground state properties and energies, STS and STM of electronically decoupled adsorbates probe excited states involving the gain or loss of an electron. For the excited states, we employ the GW approximation as a first-order perturbative correction (G_0W_0; see Methods)[23].

We will assume a ferromagnetic alignment of the two unpaired electrons, i.e. a triplet ground state, but our discussion is similarly valid for the open-shell singlet with an antiferromagnetic alignment. The resulting quasiparticle energies of the triplet state are shown in Fig. 3c. The frontier molecular orbitals are two pairs of non-disjoint, degenerate orbitals (ψ_2 and ψ_3); an occupied pair (spin up) and an unoccupied pair (spin down). The zero has been adjusted to the experimentally determined work function of monolayer Xe on Cu(111)[24] (because of the lower work function of Xe covered Cu(111) compared to NaCl covered Cu(111), the peaks are shifted downwards by 0.4 eV on bilayer NaCl on Cu(111)[25, 26]; Supplementary Fig. 10). From the level alignment, it is expected that triangulene is neutral when it adsorbs in its triplet ground state. In that case the same orbital structure is to be resolved at both voltage polarities corresponding to tunnelling out of (into) $\psi_{2\downarrow(\uparrow)}$ and $\psi_{3\downarrow(\uparrow)}$ at negative (positive) voltage. The neutral charge state of triangulene is confirmed by the experiment showing no scattering of interface electrons at triangulene on NaCl and Xe films (Supplementary Fig. 10).

In the alternative scenario of a closed-shell singlet, the frontier molecular orbitals are degenerate and half-occupied (one electron per spin channel) as shown in Supplementary Fig. 6 and a cationic charge state would be expected because of charge transfer. While we can therefore rule out the nonmagnetic closed-shell state, both magnetic states (the ferromagnetic triplet and the antiferromagnetic open-shell singlet) are compatible with our experimental results.

Fig. 3d shows the differential conductance as a function of voltage, dI/dV(V), recorded above the centre of a triangulene molecule. There is a broad voltage range in which dI/dV is essentially zero, and two distinct peaks show up at V = −1.4 V and V = 1.85 V corresponding to the positive and negative ion resonance, respectively. The satellite features observed at absolute voltages above the peaks correspond to vibronic replica[27, 26], and the negative differential conductance above the NIR stems from barrier effects[16]. The broad gap mainly stems from the Coulomb energies associated with electron removal or addition from or to the same orbitals, respectively[28]. Importantly, it is appreciably larger than a pure Coulomb gap for a system of comparable size[28], indicative for the

significant spin-splitting of triangulene.

STM images at voltages corresponding to the positive ion resonance (V = −1.4 V), the gap region (V = 0.1 V), and the negative ion resonance (V = 1.85 V) are presented in Figs. 3, e to g. The image recorded in the gap region resembles the triangular shape of triangulene. Both orbital images exhibit the same nodal plane structure, and because we know from our experiments that triangulene is neutral on Xe and on NaCl[29, 30] (see Supplementary Fig. 10) this observation suggests a magnetic ground state on these surfaces. The wave functions of the degenerate pair of occupied spin-up orbitals ($\psi_{2\uparrow}$ and $\psi_{3\uparrow}$) are plotted in Fig. 3h. Because STM probes probability densities, that is, the square of wave functions[31], we also plot the superposition of their probability densities. Similar plots for the corresponding spin-down levels, shown in Supplementary Fig. 6, look the same. In addition, Fig. 3i shows a simulated STM image, calculated by assuming an extended *s*-like wave function for the tip[29] (see Supplementary Fig. 7). The simulated image matches well the experimental orbital images at both polarities and proves that we probe the superposition of $\psi_{2\uparrow}$ and $\psi_{3\uparrow}$. Likewise, in the open-shell singlet case a superposition of $\psi_{2\uparrow}$ and $\psi_{2\downarrow}$ looks the same. That is yet another indication that we generated unsubstituted triangulene with two unpaired electrons. Importantly, DFT calculations of triangulene adsorbed on monolayer Xe on Cu(111) confirm the triplet ground state (see Supplementary Note 1).

We emphasize that our experiments demonstrate generation of stable (at our experimental conditions), unsubstituted triangulene adsorbed on three different materials, two insulator surfaces (NaCl, Xe), and, unexpectedly, also on a metal (Cu) surface. The yield of the on-surface generation method presented could likely be improved by further minimizing the time the precursor is exposed to air. Triangulene and its derivatives provide an ideal system to explore the spin-excitations within a single molecule[32], the coupling of spins between neighbouring molecules[33], the lifetime of spin states by electron paramagnetic resonance experiments[34], and are promising candidates for spintronic applications[7, 8]. In particular, it will be of great interest to exhibit (e. g. by spin-polarized STM) how the triplet ground state of triangulene is affected by its chemical environment, for example by bringing magnetic atoms close by or adsorption on ferromagnetic surfaces.

References

1. Clar, E. & Stewart, D. G. Aromatic hydrocarbons. LXV. Triangulene derivatives 1. *J. Am.*

Chem. Soc. **75,** 2667 (1953).

2. Randić, M. Aromaticity of polycyclic conjugated hydrocarbons. *Chem. Rev.* **103,** 3449 (2003).
3. Allinson, G., Bushby, R. J., Paillaud, J. L., Oduwole, D. & Sales, K. ESR spectrum of a stable triplet π biradical: trioxytriangulene. *J. Am. Chem. Soc.* **115,** 2062 (1993).
4. Allinson, G., Bushby, R. J., Jesudason, M. V., Paillaud, J. L. & Taylor, N. The synthesis of singlet ground state derivatives of non-Kekulé polynuclear aromatics. *J. Chem. Soc. Perkin Trans. 2,* 147 (1997).
5. Inoue, J. *et al.* The First Detection of a Clar's Hydrocarbon, 2,6,10-Tri-tert Butyltriangulene: A ground-state triplet of non-Kekulé polynuclear benzenoid hydrocarbon. *J. Am. Chem. Soc.* **123,** 12702 (2001).
6. Morita, Y., Suzuki, S., Sato, K. & Takui, T. Synthetic organic spin chemistry for structurally well-defined open-shell graphene fragments. *Nature Chem.* **3,** 197 (2011).
7. Bullard, Z., Girão, E. C., Owens, J. R., Shelton, W. A. & Meunier, V. Improved all-carbon spintronic device design. *Sci. Rep.* **5,** 7634 (2015).
8. Raman, K. V. *et al.* Interface-engineered templates for molecular spin memory devices. *Nature* **493,** 509 (2013).
9. Albrecht, F., Neu, M., Quest, C., Swart, I. & Repp, J. Formation and characterization of a molecule-metal-molecule bridge in real space. *J. Am. Chem. Soc.* **135,** 9200 (2013).
10. De Oteyza, D. G. *et al.* Direct imaging of covalent bond structure in single-molecule chemical reactions. *Science* **340,** 1434 (2013).
11. Ruffieux, P. *et al.* On-surface synthesis of graphene nanoribbons with zigzag edge topology. *Nature* **531,** 489 (2016).
12. Cai, J. *et al.* Atomically precise bottom-up fabrication of graphene nanoribbons. *Nature* **466,** 470 (2010).
13. Gross, L., Mohn, F., Moll, N., Liljeroth, P. & Meyer, G. The chemical structure of a molecule resolved by atomic force microscopy. *Science* **325,** 1110 (2009).
14. Pavliček, N. *et al.* On-surface generation and imaging of arynes by atomic force microscopy. *Nature Chem.* **7,** 623 (2015).
15. Schuler, B. *et al.* Reversible Bergman cyclization by atomic manipulation. *Nature Chem.* **8,** 220 (2016).
16. Repp, J., Meyer, G., Stojković, S. M., Gourdon, A. & Joachim, C. Molecules on insulating films: Scanning-tunneling microscopy imaging of individual molecular orbitals. *Phys. Rev. Lett.* **94,** 026803 (2005).
17. Mistry, A. *et al.* The synthesis and STM/AFM imaging of "Olympicene" benzo[*cd*]pyrenes. *Chem. Eur. J.* **21,** 2011 (2014).
18. Schuler, B. *et al.* Adsorption geometry determination of single molecules by atomic force microscopy. *Phys. Rev. Lett.* **111,** 106103 (2013).
19. Gaudioso, J., Lee, H. J. & Ho, W. Vibrational analysis of single molecule chemistry: Ethylene dehydrogenation on Ni(110). *J. Am. Chem. Soc.* **121,** 8479 (1999).

20. Bordwell, F. G., Cheng, J. P., Satish, A. V. & Twyman, C. L. Acidities and hemolytic bond dissociation energies (BDEs) of benzyl-type carbon-hydrogen bonds in sterically congested substrates. *J. Org. Chem.* **57,** 6542 (1992).
21. Van Scheppingen, W., Dorrestijn, E., Arends, I., Mulder, P. & Korth, H.-G. Carbon-Oxygen bond strength in diphenyl ether and phenyl vinyl ether: An experimental and computational study. *J. Phys. Chem. A* **101,** 5404 (1997).
22. Sonnleitner, T., Swart, I., Pavliček, N., Pöllmann, A. & Repp, J. Molecular symmetry governs surface diffusion. *Phys. Rev. Lett.* **107,** 186103 (2011).
23. Hedin, L., New method for calculating the one-particle Green's function with application to the electron-gas problem, *Phys. Rev.* **139**, A796 (1965).
24. Wolf, M., Knoesel, E. & Hertel, T. Ultrafast dynamics of electrons in image-potential states on clean and Xe-covered Cu(111). *Phys. Rev. B* **54,** R5295 (1996).
25. Bennewitz, R. *et al.* Aspects of dynamic force microscopy on NaCl/Cu(111): resolution, tip-sample interactions and cantilever oscillation characteristics. *Surface and Interface Analysis* **27,** 462 (1999).
26. Pavliček, N., Repp, J., Swart, I., Meyer, G. & Niedenführ, J. Symmetry dependence of vibration-assisted tunneling. *Phys. Rev. Lett.* **110,** 136101 (2013).
27. Qiu, X. H., Nazin, G. V. & Ho, W. Vibronic states in single molecule electron transport. *Phys. Rev. Lett.* **92,** 206102 (2004).
28. Repp, J., Meyer, G., Paavilainen, S., Olsson, F. E. & Persson, M. Imaging bond formation between a gold atom and pentacene on an insulating surface. *Science* **312,** 1196 (2006).
29. Repp, J., Meyer, G., Olsson, F. E. & Persson, M. Controlling the charge state of individual gold adatoms. *Science* **305,** 493 (2004).
30. Swart, I., Sonnleitner, T. & Repp, J. Charge state control of molecules reveals modification of the tunneling barrier with intramolecular contrast. *Nano Lett.* **11,** 1580 (2011).
31. Tersoff, J. & Hamann, D. R. Theory of the scanning tunneling microscope. *Phys. Rev. B* **31,** 805 (1985).
32. Heinrich, A. J., Gupta, J. A., Lutz, C. P. & Eigler, D. M. Single-atom spin-flip spectroscopy. *Science* **306,** 466 (2004).
33. Hirjibehedin, C. F., Lutz, C. P. & Heinrich, A. J. Spin coupling in engineered atomic structures. *Science* **312,** 1021 (2006).
34. Baumann, S. *et al.* Electron paramagnetic resonance of individual atoms on a surface. *Science* **350,** 417 (2015).

Acknowledgments

We acknowledge Rolf Allenspach, Diego Peña, Jascha Repp, and Ivano Tavernelli for valuable comments on the manuscript. The research leading to these results received funding from the ERC Advanced Grant CEMAS (agreement no. 291194), the ERC Consolidator Grant AMSEL (682144), the EU project PAMS (610446) and the ITN QTea (317485).

Author contributions

N. P., Z. M., L. G. and G. M. performed the STM/AFM experiments; N. P. and N. M. performed the DFT calculations; A. M. and D. J. F. synthesized the precursor molecules; all authors analysed the data and contributed to the manuscript.

Competing financial interests

The authors declare no competing financial interests.

Data availability statement

The data that support the findings of this study are available from the corresponding author upon reasonable request.

Additional information

Supplementary information is available in the online version of the paper. Reprints and permission information is available online at www.nature.com/reprints. Correspondence and requests for materials should be addressed to N. P. or D. J. F.

Figure Captions

Figure 1: Scheme illustrating the generation of triangulene **1**.

Removal of two H atoms by means of atomic manipulation from dihydrodibenzo[*cd,mn*]pyrene (**2)** results in triangulene (**1**). Isomers **2a** and **2b** are energetically most favourable, while **2c** and **2d** are possible isomers with higher energies. Structures **3** and **4** show related ketones. Aromatic cores are highlighted.

Figure 2: Comparison of different molecular species on NaCl.

a-d, STM images (imaging parameters I = 1 pA, V = 0.1 V) of four molecular species acquired with CO-terminated tips (CO tips). **e-h,** Corresponding AFM images (constant-height offsets with respect to the STM set point above NaCl were Δz = −1.4 Å, −1.65 Å, −1.3 Å, and −2.1 Å, respectively) are shown below. Scale bars, 5 Å.

Figure 3: Characterization of triangulene on Cu and Xe.

a,b, AFM images of triangulene on Cu (Δz = 1.66 Å, I_{sp} = 2 pA, V_{sp} = 0.1 V) and Xe (Δz = −0.82 Å, I_{sp} = 1 pA, V_{sp} = 0.1 V), respectively. **c,** Energy level scheme derived from spin-polarized DFT calculations in the G_0W_0 approximation. **d,** STS performed at the centre of a triangulene molecule on Xe showing the tunnelling current (red) and the differential conductance dI/dV (blue) as a function of voltage. **e-g,** STM images at voltages corresponding to the positive ion resonance (PIR), the gap region, and the negative ion resonance (NIR), respectively (I = 2 pA). **h,** Plots of the DFT-calculated wave functions $\psi_{2\uparrow}$ and $\psi_{3\uparrow}$ and the sum of their probability densities ($|\psi_{2\uparrow}|^2 + |\psi_{3\uparrow}|^2$). **i,** Simulated STM image of degenerate orbitals $\psi_{2\uparrow}$ and $\psi_{3\uparrow}$ probed with a *s*-like tip wave function ψ_S. Scale bars, 5 Å.

Methods

Synthesis

Compound **2** has been synthesized using the procedure presented in Supplementary Fig. 1, and was immediately transferred to ultrahigh vacuum to minimize its oxidation[1]. Details on the synthesis and spectroscopic characterization of all compounds and necessary precursors are given in the Supplementary Methods.

STM/AFM experiments

The experiments were carried out in a homebuilt combined STM and AFM operating under ultrahigh vacuum conditions (base pressure $p < 10^{-10}$ mbar) at a temperature $T = 5$ K. The microscope was equipped with two different qPlus sensors[35, 36] with eigenfrequencies of $f_0 = 31036$ Hz and 25035 Hz, respectively, a stiffness of $k = 1800$ N/m and Q factors on the order of 10^5. The voltage V was applied to the sample. The AFM was operated in frequency-modulation mode[37] at an oscillation amplitude of $A = 50$ pm.

STM images were recorded in constant-current mode (closed feedback loop) and show the topography z. AFM images were performed in constant-height mode (open feedback loop) and show the frequency shift Δf. A height offset Δz with respect to an indicated STM set point above the bare surface (Cu, NaCl, Xe) is given for each AFM image. Positive height offsets refer to a distance decrease. STS (that is, $I(V)$ curves) was also performed in constant-height mode. The differential conductance, $dI/dV\,(V)$, was then obtained by numerical differentiation of the $I(V)$ signal.

STM and AFM images, as well as numerically obtained $dI/dV(V)$ curves were post-processed using Gaussian low-pass filters (FWHM corresponding to 4-6 pixels for raw data of 160 × 160 to 640 × 640 pixels).

The tip had been terminated with a CO molecule for all AFM images. STM images and STS spectra were acquired with metal-terminated tips, except where stated otherwise. CO molecules were picked up from NaCl islands, or on Xe monolayers (ML) from step edges to two-layer-thick Xe islands.

Sample preparation

Cu(111) single crystals were cleaned by sputtering and annealing cycles. Experiments were performed on the bare Cu(111) surface, on 2 ML thick islands of NaCl and on 1-ML-thick islands of Xe.

NaCl islands were grown by sublimation from a crucible onto the cleaned Cu(111) surface held at a temperature of 270 K[38]. This resulted in (100)-terminated NaCl islands of 2 to 3 ML thickness.

Closed-packed Xe films were grown by Xe adsorption onto the Cu(111) crystal while the sample was inside the microscope head at temperatures below 15 K. A background Xe pressure of 2×10^{-5} mbar was maintained in

the UHV chamber, and a shutter to the microscope head was opened for about 30 s. This resulted in Xe islands of 1 to 2 ML thickness.

Precursor molecules (**2**) were thermally sublimed in a two-step procedure. First, the compound was filled into crucibles made from tantalum directly after synthesis, which were inserted into the load-lock of the UHV chamber, and evacuated to a pressure better than 10^{-4} mbar. To minimize oxidation, the entire process was carried out speedily, taking less than 30 minutes in total from synthesis until evacuation. Next, the compound was sublimed from the crucible onto a mobile evaporator in the load-lock (at $p \sim 10^{-8}$ mbar) of the UHV chamber. Then, this evaporator was introduced into the STM chamber ($p < 10^{-10}$ mbar), and the compound was deposited by means of flash sublimation onto the cold sample (below 10 K) placed in the microscope head. In addition, low coverages of CO molecules (for tip preparation) were dosed onto the cold sample.

DFT calculations

DFT calculations[39] were performed using the FHI-aims code with numerical atomic orbitals as the basis functions[40] and the Perdew-Burke-Ernzerhof (PBE) exchange-correlation functional[41] was applied for all calculations. A van der Waals method (Tkatchenko-Scheffler)[42] combined with the Lifshitz-Zaremba-Kohn theory for the non-local Coulomb screening within the bulk for the Cu substrate[43] was used. The default *tight* basis sets were used for all calculations, except for the calculations of free triangulene, for which the *really-tight* sets were used. The GW method[23, 44, 45] was applied to account for many-body effects. This approach has been reported to accurately predict band gaps of graphene nanoribbons[46] or molecules[47, 48].

The total energies, electron densities and molecular orbitals were calculated for the free molecules (triangulene and hydrogenated derivatives, see Supplementary Table 1 and Supplementary Fig. 2) and the adsorption geometries for triangulene on 1 ML Xe on Cu(111), which is shown in Supplementary Fig. 3. Plots of the projected density of states for free triangulene in its different magnetic states and for triangulene adsorbed on Xe are shown in Supplementary Fig. 4.

The energy of the (ferromagnetic) triplet state was calculated by performing unrestricted spin-polarised energy minimization. To select the (antiferromagnetic) open-shell singlet state two spatially separated initial magnetic moments of opposing sign were defined. To select the (nonmagnetic) closed-shell singlet state the spin of the entire unit cell was constrained to a spin multiplicity of one or spin-unpolarised calculations were performed. In all cases the geometry was optimized independently until the atomic force components per atom converged to less than 10^{-4} eV/Å.

The slab to model the (111) surface consisted of four layers of Cu. The (x, y, z) dimension of the hexagonal cell was (15.30 Å, 15.30 Å, 50 Å). The Xe layer and the two topmost Cu layers were fully relaxed. The first Brillouin zone was sampled by 2x2 k-points.

References for the Methods section

35. Giessibl, F. J. High-speed force sensor for force microscopy and profilometry utilizing a quartz tuning fork. *Appl. Phys. Lett.* **73,** 3956 (1998).
36. Giessibl, F. J. Advances in atomic force microscopy. *Rev. Mod. Phys.* **75,** 949 (2003).
37. Albrecht, T. R., Grütter, P., Horne, D. & Rugar, D. Frequency modulation detection using high-Q cantilevers for enhanced force microscope sensitivity. *J. Appl. Phys.* **69,** 668 (1991).
38. Bennewitz, R., Foster, A. S., Kantorovich, L. N. & Bammerlin, M. Atomically resolved edges and kinks of NaCl islands on Cu(111): Experiment and theory. *Phys. Rev. B* **62,** 2074 (2000).
39. Hohenberg, P. & Kohn, W. Inhomogeneous electron gas. *Phys. Rev.* **136,** B864 (1964).
40. Blum, V. *et al.* Ab initio molecular simulations with numeric atom-centered orbitals. *Comp. Phys. Comm.* **180,** 2175 (2009).
41. Perdew, J. P., Burke, K. & Ernzerhof, M. Generalized gradient approximation made simple. *Phys. Rev. Lett.* **77,** 3865 (1996).
42. Tkatchenko, A. & Scheffler, M. Accurate molecular van der Waals interactions from ground-state electron density and free-atom reference data. *Phys. Rev. Lett.* **102,** 073005 (2009).
43. Onida, G., Reining, L., and Rubio, A., Electronic excitations: density-functional versus many-body Green's-function approaches, *Rev. Mod. Phys.* **74**, 601 (2002).
44. Ruiz, V. G., Liu, W., Zojer, E., Scheffler, M. & Tkatchenko, A. Density-functional theory with screened van der Waals interactions for the modeling of hybrid inorganic-organic systems. *Phys. Rev. Lett.* **108,** 146103 (2012).
45. Ren, X. *et al.* Resolution-of-identity approach to Hartree–Fock, hybrid density functionals, RPA, MP2 and GW with numeric atom-centered orbital basis functions. *New Journal of Physics* **14,** 053020 (2012).
46. Yang, L., Park, C.-H., Son, Y.-W., Cohen, M. L. & Louie, S. G. Quasiparticle energies and band gaps in graphene nanoribbons. *Phys. Rev. Lett.* **99,** 186801 (2007).
47. Rostgaard, C., Jacobsen, K. W. & Thygesen, K. S. Fully self-consistent GW calculations for molecules. *Phys. Rev. B* **81,** 085103 (2010).
48. Neaton, J. B., Hybertsen, M. S. & Louie, S. G. Renormalization of molecular electronic levels at metal-molecule interfaces. *Phys. Rev. Lett.* **97**, 216405 (2006).

1 triangulene

-2 H

-2 H

2a

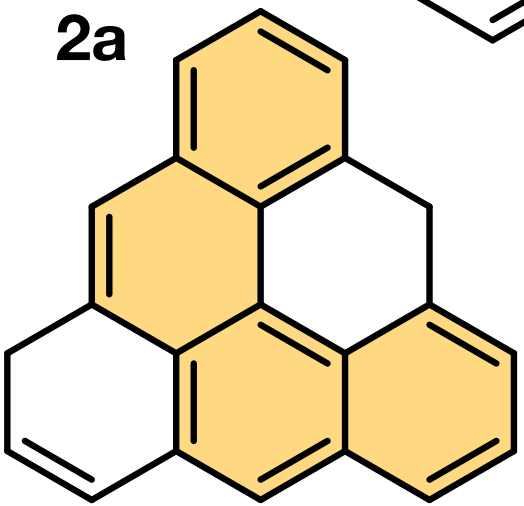

2b

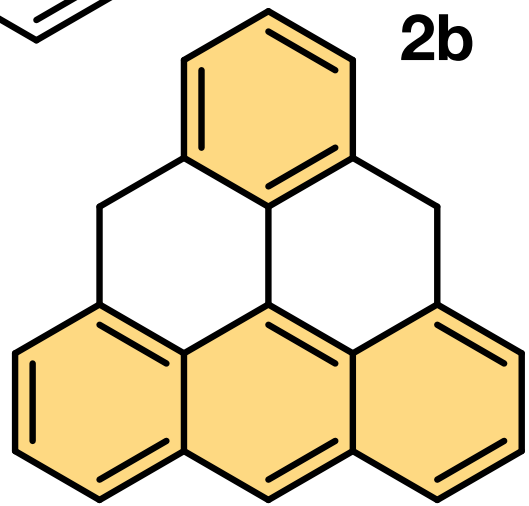

2c

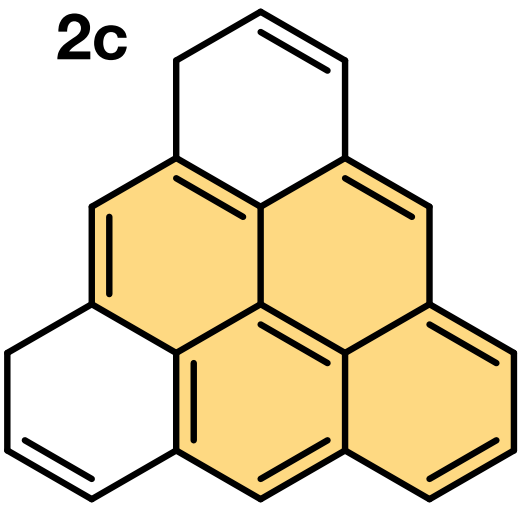

2d

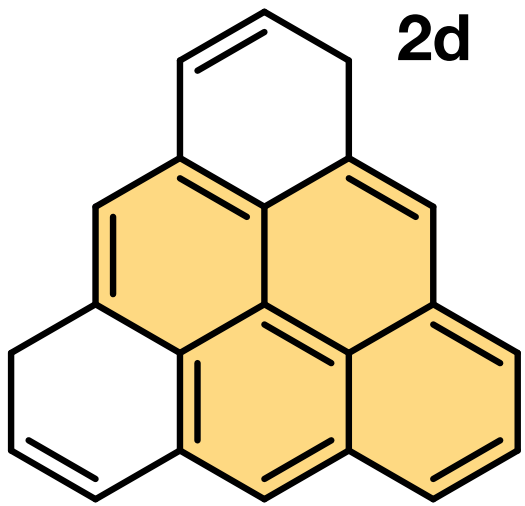

ketones

3

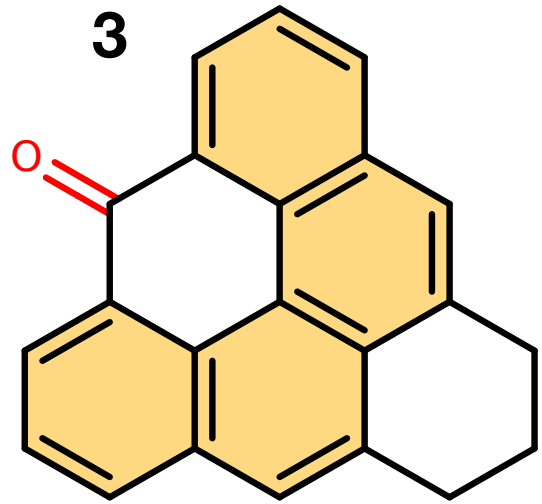

4

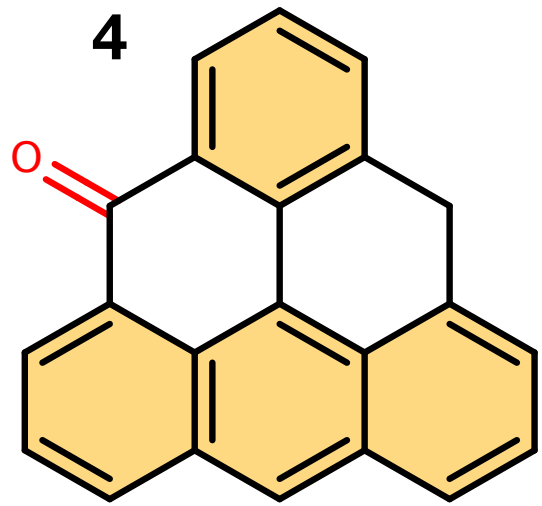

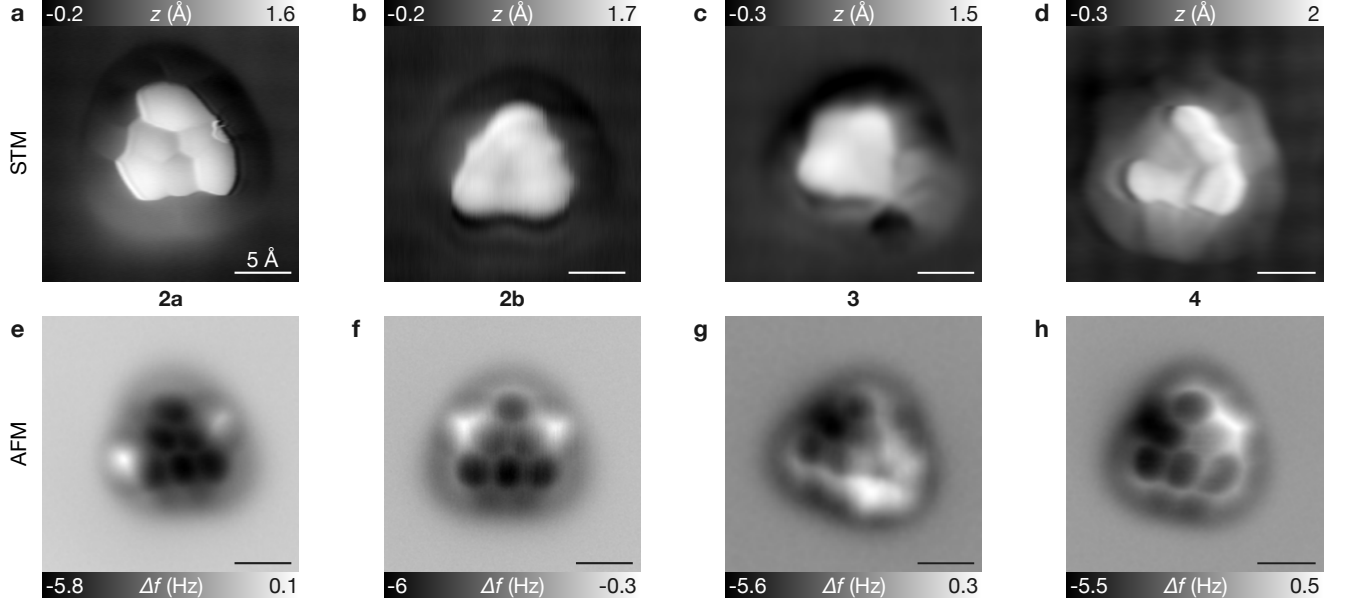
a
-0.2
z (Å)
1.6
5 Å
b
-0.2
z (Å)
1.7
c
-0.3
z (Å)
1.5
d
-0.3
z (Å)
2
STM
2a
2b
3
4
e
f
g
h
AFM
-5.8
Δf (Hz)
0.1
-6
Δf (Hz)
-0.3
-5.6
Δf (Hz)
0.3
-5.5
Δf (Hz)
0.5

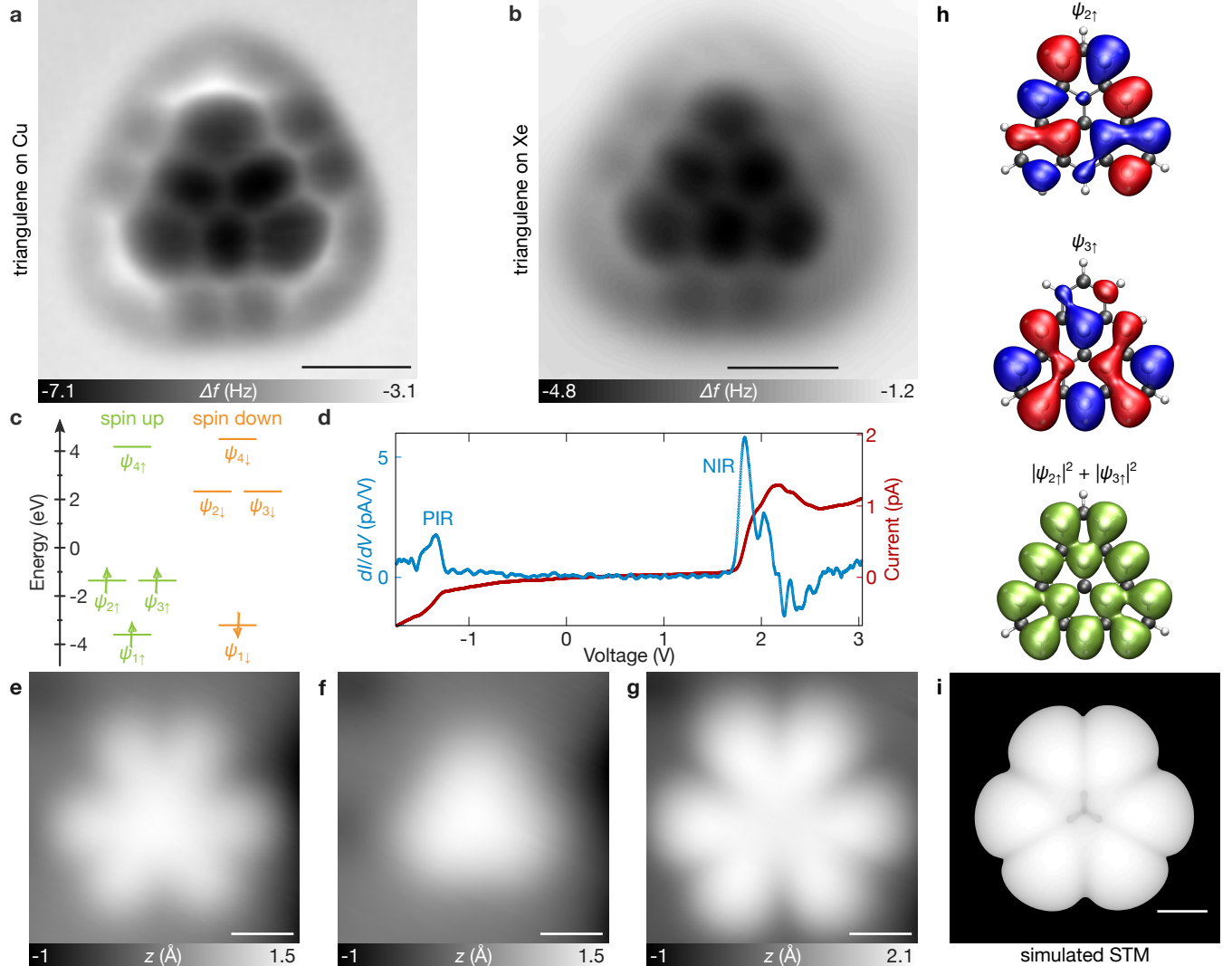
a
triangulene on Cu
-7.1
Δf (Hz)
-3.1
b
triangulene on Xe
-4.8
Δf (Hz)
-1.2
h
ψ2↑
ψ3↑
|ψ2↑|2 + |ψ3↑|2
c
spin up
spin down
Energy (eV)
4
2
0
-2
-4
ψ4↑
ψ4↓
ψ2↓
ψ3↓
ψ2↑
ψ3↑
ψ1↑
ψ1↓
d
dI/dV (pA/V)
Current (pA)
PIR
NIR
Voltage (V)
e
-1
z (Å)
1.5
f
-1
z (Å)
1.5
g
-1
z (Å)
2.1
i
simulated STM

Synthesis and characterization of triangulene

Niko Pavliček, Anish Mistry, Zsolt Majzik, Nikolaj Moll, Gerhard Meyer, David J. Fox, Leo Gross

Contents

Supplementary Methods

Experimental synthetic chemistry: synthesis of precursor molecules 2

Reactions were carried out at room temperature unless otherwise stated. Column chromatography purifications were carried out using silica gel LC60A40-63 micron. Melting points were recorded twice on a Stuart SM10 instrument. Infrared spectra were recorded on a Perkin-Elmer paragon 1000 FT-IR spectrophotometer. Hydrogen and carbon NMR were recorded on a Bruker Advanced DRX-500 MHz, Fourier transform spectrometers and all samples were submitted in deuterated $CDCl_3$ unless otherwise stated. Coupling constant values *J* are rounded to the nearest 0.5 Hz. Hydrogen-decoupled carbon NMR spectra were taken using PENDANT (polarization enhancement during attached nucleus testing), HMQC (heteronuclear multiple quantum coherence) and COSY (correlation spectroscopy) to further assist in compound analysis. Mass spectra were obtained on a micrOTOF 87 instrument using mass electrospray ionization with positive ion polarity unless otherwise stated.

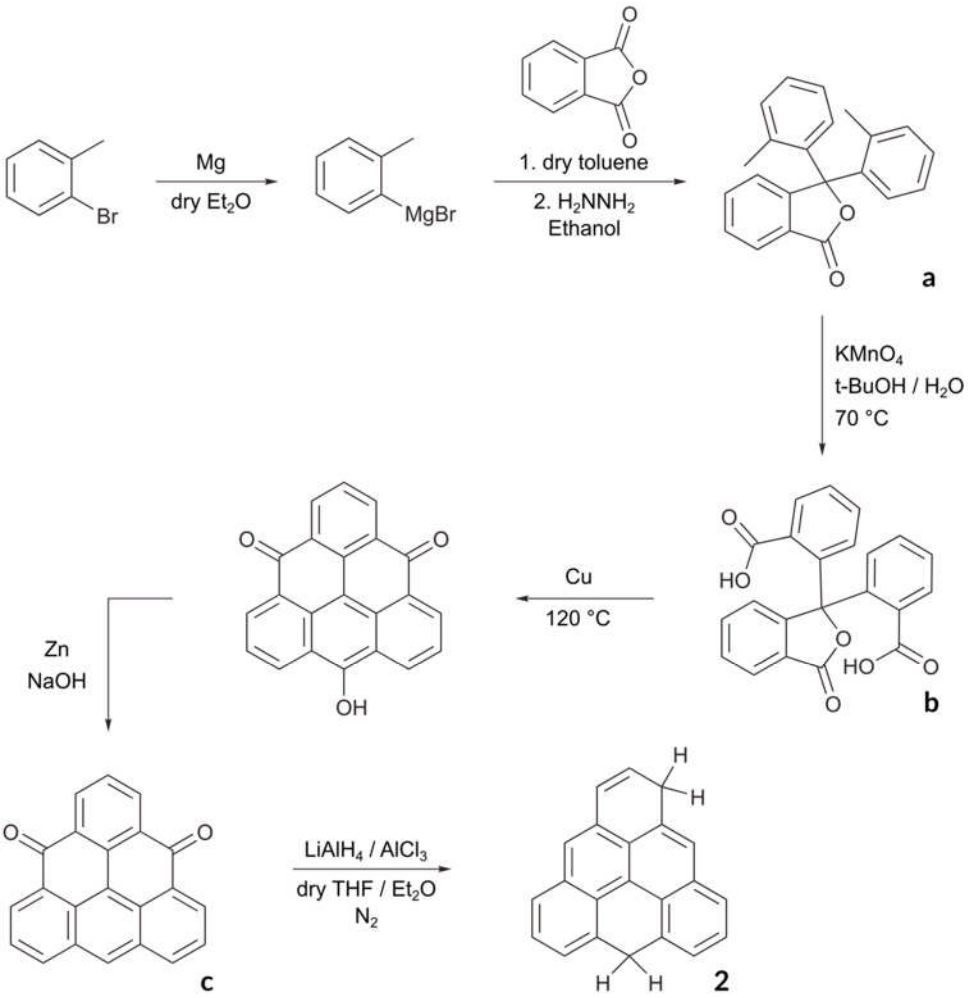

Supplementary Fig. 1. Scheme illustrating the synthesis of compound **2.** For the STM/AFM experiments, the last step (from **c** to **2**) was carried out directly before putting the compound into the load-lock of the apparatus.

3,3-Di-o-tolyl-1,3-dihydro-2-benzofuran-1-one (**a**)

This method was taken from previous literature[1,49] and the data is consistent with ref. 49.

Dry diethyl ether (170 ml) was added to magnesium turnings (8.82 g, 0.363 mol) under a nitrogen atmosphere *via* a cannula. The solution was refluxed and 2-bromotoluene (40 ml, 0.330 mol) was added drop-wise and the solution was left to reflux for a further 3 hours. In a separate flask, dry toluene (280 ml) was added *via* a cannula to solid phthalic anhydride (20 g, 0.130 mol) under a nitrogen atmosphere. The *o*-tolylmagnesium bromide was then slowly added into the phthalic anhydride solution *via* a cannula and the reaction was left to reflux for a day and a half. The reaction was cooled and quenched with 2M HCl (250 ml) on an ice bath. The organics were collected and washed with water (3 × 200 ml), dried with

sodium sulphate and organics were removed under vacuum to provide a crude viscous orange residue.

The viscous orange residue was dissolved in ethanol (250 ml), hydrazine monohydrate was added (8.6 ml) and the reaction was refluxed for 24 hours. Ethanol was removed under vacuum and the solid was collected and washed with cold ethanol (3 × 20 ml), which was subsequently left to dry in a desiccator to obtain a pure off-white powder (9.25 g, 22%).

IR spectroscopy

ν_{max} = 1755 (C=O ester), 1597 (C=C), 1463 (CH deformations), 1118, 691 (benzene rings) cm^{-1}.

Melting point

T_{mp} = 171 °C to174 °C.

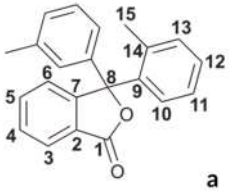

a

^{1}H NMR data (500 MHz, $CDCl_3$)

δ_H 7.96 (1H, d, *J* = 7.5 Hz, H-3), 7.68 (1H, td, *J* = 7.5, 1.0 Hz, H-5), 7.56 (1H, td, *J* = 7.5, 0.5 Hz, H-4), 7.39 (1H, d, *J* = 7.5 Hz, H-6), 7.23 (2H, td, *J* = 7.5, 1.0 Hz, H-12), 7.17 (2H, br. d, *J* = 7.0 Hz, H-13), 7.09 (2H, td, *J* = 7.5, 1.0 Hz, H-11), 7.02 (2H, dd, *J* = 8.0, 0.5 Hz, H-10), 2.14 (6H, s, H-15) ppm.

^{13}C NMR data (125 MHz, $CDCl_3$)

δ_C 170.0 (C-1), 151.3 (C-7), 138.8 (C-9), 137.3 (C-14), 133.9 (C-5), 132.8 (C-13), 129.2 (C-4), 128.5 (C-12), 127.1 (C-10), 126.5 (C-2), 125.7 125.7 (C-3, -11), 125.2 (C-6), 94.1 (C-8), 21.5 (C-15) ppm.

Mass spectrometry

m/z calculated 337.1199 for $C_{22}H_{18}O_2Na$ (M+Na), found 337.1200.

Di-(*o*-carboxyphenyl)-phthalide (**b**)

This method was taken from previous literature[1,50] and the data (without NMR) is consistent with ref. 1.

$KMnO_4$ (1.26 g, 7.97 mmol, 2.5 eq.) was added portion-wise to a stirring solution of (**a**) in *t*-BuOH/H_2O (1:1, 10 ml). The mixture was heated to 70 °C for 2 hours and then the reaction was cooled to room temperature and more $KMnO_4$ (1.26 g, 7.97 mmol, 2.5 eq.) was added portion-wise. The solution was then heated to 70 °C and was left to react overnight. The hot reaction mixture was filtered through a pad of celite and washed through with hot water. The water in the filtrate was removed under vacuum to approximately 10% of its original volume. The residue was then acidified in an ice bath with concentrated HCl to pH 2 to form a precipitate. The precipitate was collected and dried in a desiccator to obtain a crystalline white solid (0.86 g, 72%).

IR spectroscopy

ν_{max} = 3072 (OH), 1745 (C=O ester), 1712 (C=O acid) 1596 (C=C), 1115, 693 (benzene rings) cm^{-1}.

Melting point

T_{mp} = 255 °C to 261 °C.

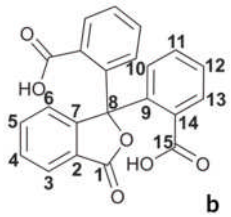

b

^{1}H NMR data (500 MHz, DMSO)

δ_H 12.72 (2H, br. s, OH), 7.85 (1H, br. d, *J* = 7.5 Hz, H-3), 7.80 (1H, br. d, *J* = 7.5 Hz, H-6), 7.77 (1H, td, *J* = 7.5, 1.0 Hz, H-5), 7.63 (1H, td, *J* = 7.5, 1.0 Hz, H-4), 7.48-7.45 (2H, m, H-13), 7.43-7.37 (2H, m, H-11, -12), 7.24-7.20 (2H, m, H-10) ppm.

^{13}C NMR data (125 MHz, DMSO)

δ_C 169.5 (C-15), 168.9 (C-1), 151.3 (C-7), 137.9 (C-9), 133.9 (C-5), 132.9 (C-14), 129.6 (C-4), 129.5 (C-11 or -12), 129.1 (C-13), 128.2 (C-10 or -11 or -12), 128.1 (C-10 or -11 or -12), 125.7 (C-2), 125.2 (C-3 or -6), 125.1 (C-3 or -6), 90.5 (C-8) ppm.

Mass spectrometry

m/*z* calculated 397.0683 for $C_{22}H_{14}O_6Na$ (M+Na), found 397.0680.

4,8-Dioxo-4*H*,8*H*-dibenzo[*cd*,*mn*]pyrene (**c**)

This method was taken from previous literature[1,4,49] and the data is consistent with ref. 4.

Copper powder (0.22 g, 3.5 mmol) and sulphuric acid (7 ml) were added to (**b**) (0.77 g, 2.06 mmol) and heated to 120 °C for 2 hours. The mixture was filtered hot through sintered glass. The solution was cooled and then cold water (5 ml) was added, thereafter the dark blue precipitate was collected by filtration. The blue precipitate was then dissolved in minimum dilute 2M NaOH (30 ml) with zinc dust added (1.5 g); the mixture was left to stir under a nitrogen atmosphere. This was stirred (0.5 to 1 h) until on exposure to air, the solution did not go back to a dark blue colour when left for about 5 minutes. The solution was then filtered and air was bubbled through it for approximately 15 minutes where a precipitate was observed. Concentrated HCl was added and the red solution was partitioned with DCM (3 × 40 ml), organics were collected and dried with sodium sulphate. The dark red crude solid was purified by column chromatography (chloroform:ethyl acetate = 9:1) to obtain a pure red solid (22 mg, 35%).

IR spectroscopy

ν_{max} = 2918, 2848 (CH), 1644 (C=O), 1576 (C=C), 1220, 948, 750 (benzene rings) cm^{-1}.

Melting point

T_{mp} > 300 °C.

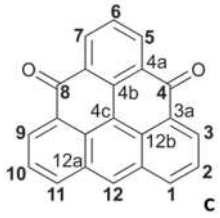

c

^{1}H NMR (500 MHz, $CDCl_3$)

δ_H 8.96 (2H, dd, *J* = 7.0, 1.0 Hz, H-3), 8.84-8.82 (3H, m, H-5, H-12), 8.49 (2H, br. d, *J* = 8.0 Hz, H-1), 7.89 (2H, dd, *J* = 8.0, 7.0 Hz, H-2), 7.81 (1H, t, *J* = 7.5 Hz, H-6) ppm.

^{13}C NMR data (125 MHz, $CDCl_3$)

δ_C 182.9 (C-4), 136.3 (C-1), 135.5 (C-4b), 133.3 (C-3 or -5), 133.0 (C-3 or -5), 132.4 (C- 12), 130.9 (C-3a or -12a), 130.7 (C-4a), 128.7 (C-3a or -12a), 128.2 (C-6), 126.7 (C-2), 126.7 (C-12b), 116.7 (C-4c) ppm.

Mass spectrometry

m/z calculated 329.0573 for $C_{22}H_{10}O_2Na$ (M+Na), found 329.0575.

3,8-Dihydro-*3H,8H*-dibenzo[*cd,mn*]pyrene (**2**)

The method was taken from previous literature and the data is consistent with it [51].

Compound **c** (20 mg, 0.065 mmol) in dry THF (5 ml) was added drop-wise under a nitrogen atmosphere to a stirring solution of $LiAlH_4$ (9.90 mg, 0.261 mmol, 4 eq.) and $AlCl_3$ (0.069 g, 0.522 mmol, 8 eq.) in dry diethyl ether (5 ml) in an ice bath. The reaction was then left at room temperature for 1.5 h to react. The solvent was removed under vacuum, DCM was added (5 ml), and water and then aqueous HCl (1:3) were added to the reaction sequentially under a nitrogen atmosphere. The organics were collected and were dried with sodium sulphate. This was then filtered through a silica plug, and the organics were reduced under vacuum to produce an air-sensitive, light pink solid (17 mg, 93%).

IR spectroscopy

ν_{max} = 2953, 2919, 2849 (CH), 1585 (C=C), 1231, 930, 751 (benzene rings), 710 (CH_2 rocking) cm^{-1}.

Melting point

T_{mp} = 182 °C to 185 °C.

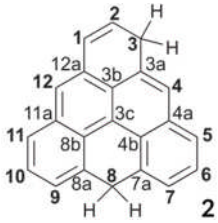

^{1}H NMR (500 MHz, $CDCl_3$)

δ_H 7.94 (1H, d, *J* = 8.0 Hz, H-5), 7.58 (1H, d, *J* = 8.0 Hz, H-11), 7.53 – 7.49 (1H, m, H-6), 7.47 (1H, s, H-4 or 12), 7.41 (1H, dd, *J* = 7.0, 1.0 Hz, H-7), 7.40 -7.36 (1H, m, H-10), 7.35 (1H, s, H-4 or 12), 7.32 (1H, dd, *J* = 7.0, 1.0 Hz, H-9), 6.74 (1H, dt, *J* = 10.0, 2.0 Hz, H-1), 6.18 (1H, dt, *J* = 10.0, 4.0 Hz, H-2), 4.87 (2H, br s, H-8), 3.90 (2H, br s, H-3) ppm.

^{13}C NMR data (125 MHz, $CDCl_3$)

δ_C 146.2 (C-3a or -3b or -3c), 134.3 (C-7a), 133.0 (C-8a), 131.1 (C-11a), 129.4 (C-12a), 128.1 (C-8b), 127.9 (C-1), 127.6 (C-4b), 126.2 (C-6), 125.8 (C-2 or -10), 125.7 (C-2 or -10), 125.3 (C-11), 125.1 (C-

7), 124.8 (C-9), 124.6 (C-3a or -3b or -3c), 123.9 (C-4a), 123.7 (C-4 or -12), 118.0 (C-5), 111.7 (C-3a or -3b or -3c), 34.2 (C-8), 26.6 (C-3) ppm, *one peak missing due to overlapping peaks (C-4 or -12).

Mass spectrometry

m/z calculated 279.1168 for $C_{22}H_{15}$ (M+H), found 279.1168.

NMR spectra of all compounds

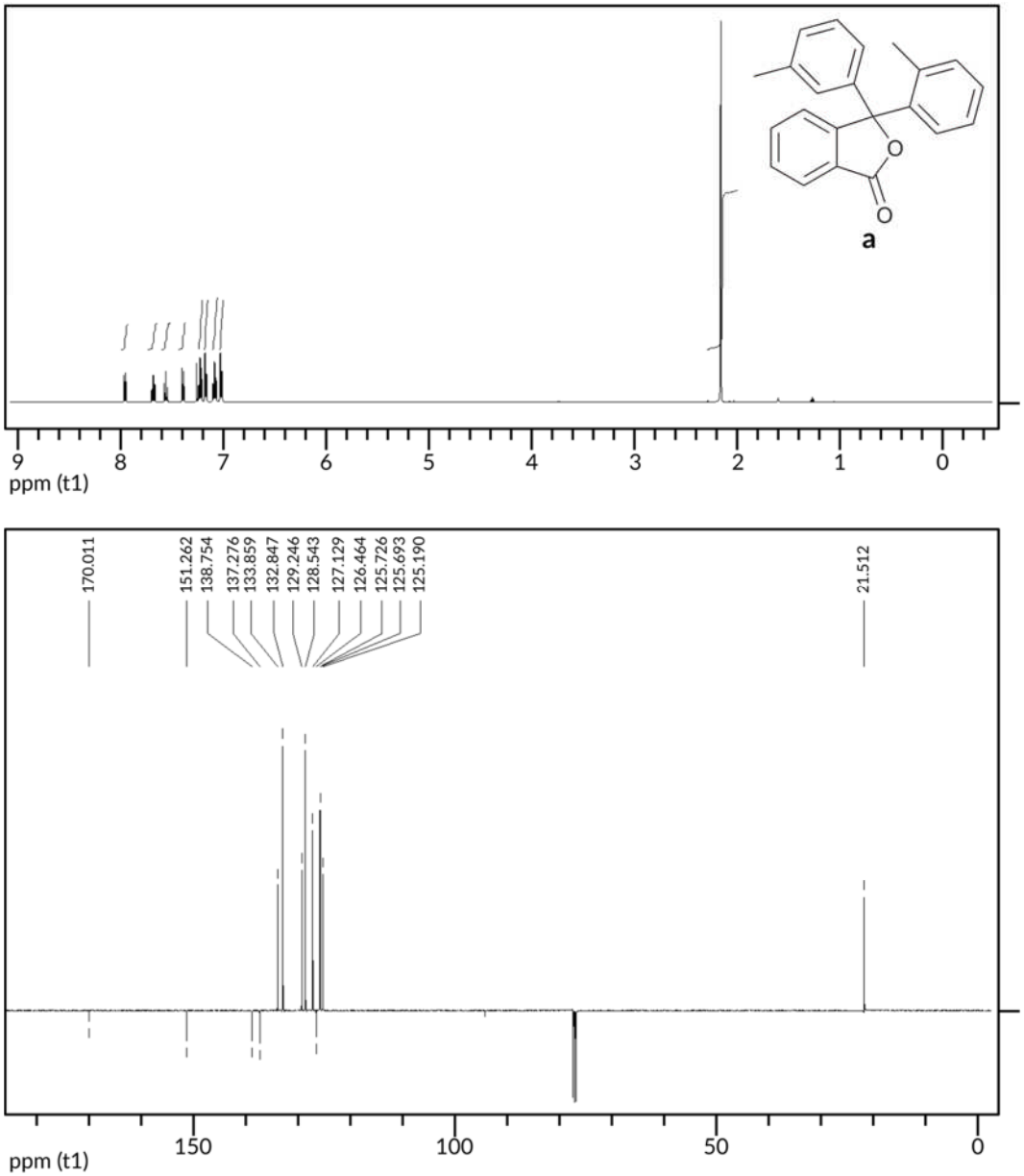

^{1}H (top) and ^{13}C (bottom) NMR spectra of compound **a**.

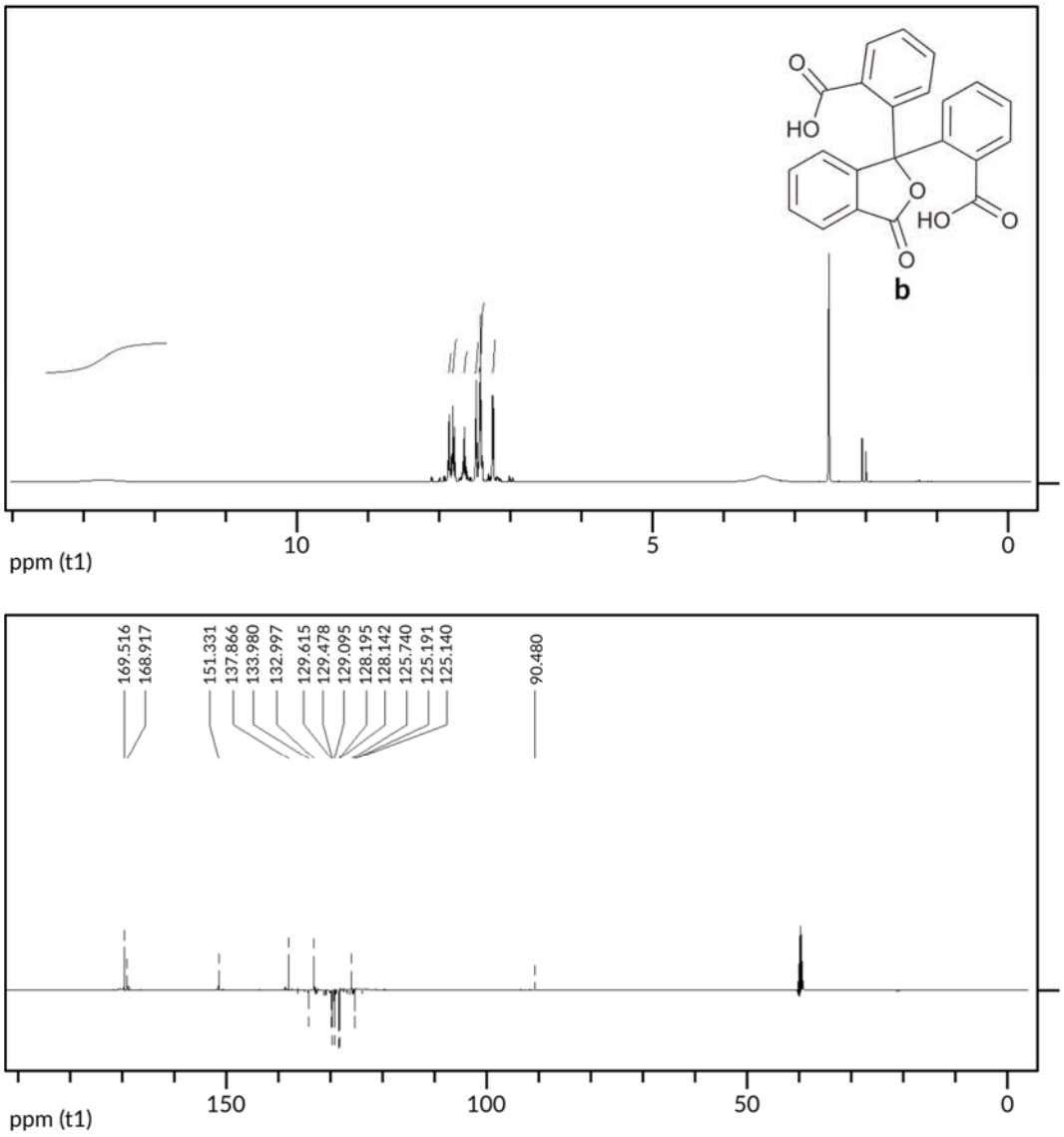

^{1}H (top) and ^{13}C (bottom) NMR spectra of compound **b**.

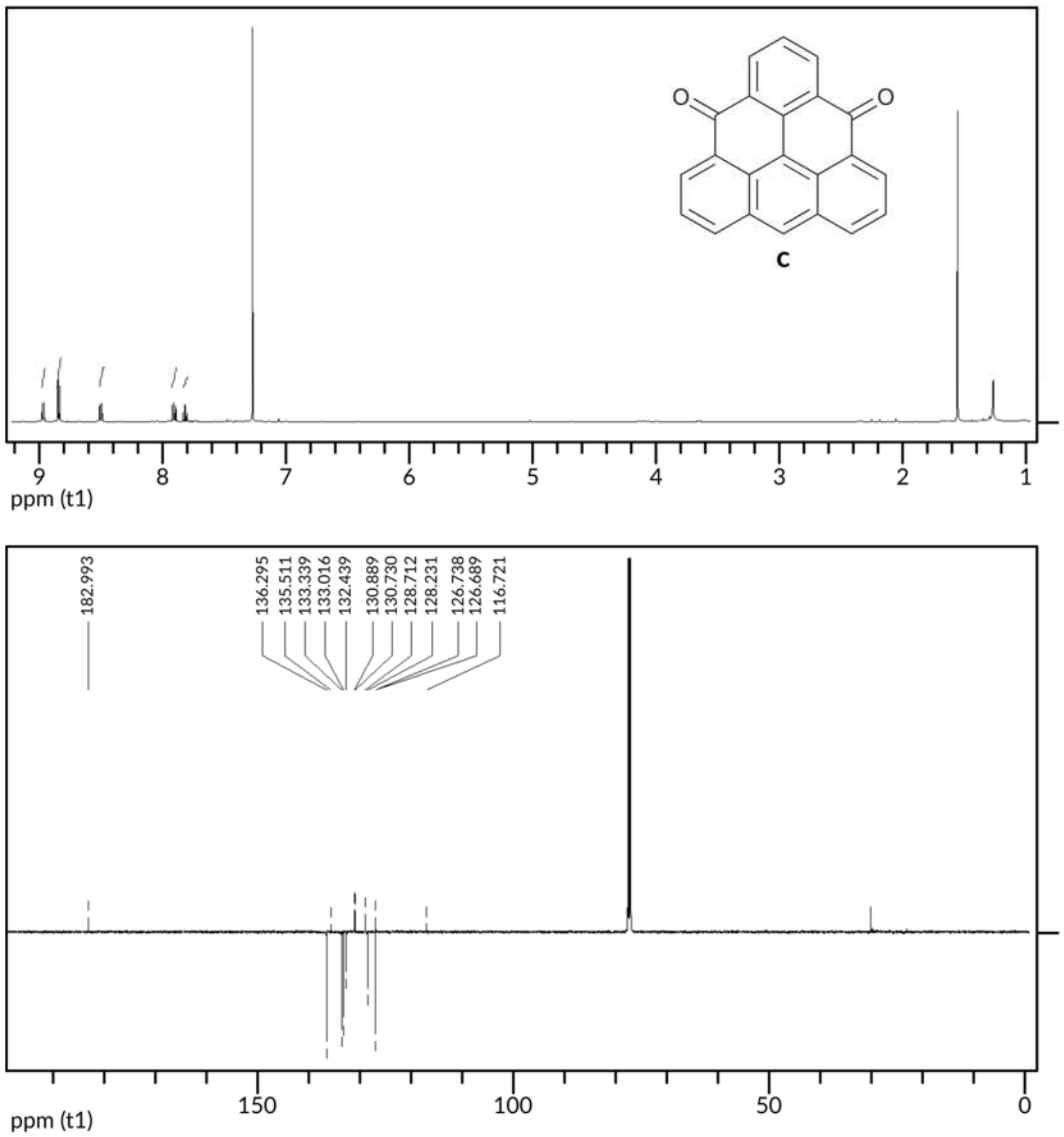

^{1}H (top) and ^{13}C (bottom) NMR spectra of compound **c**.

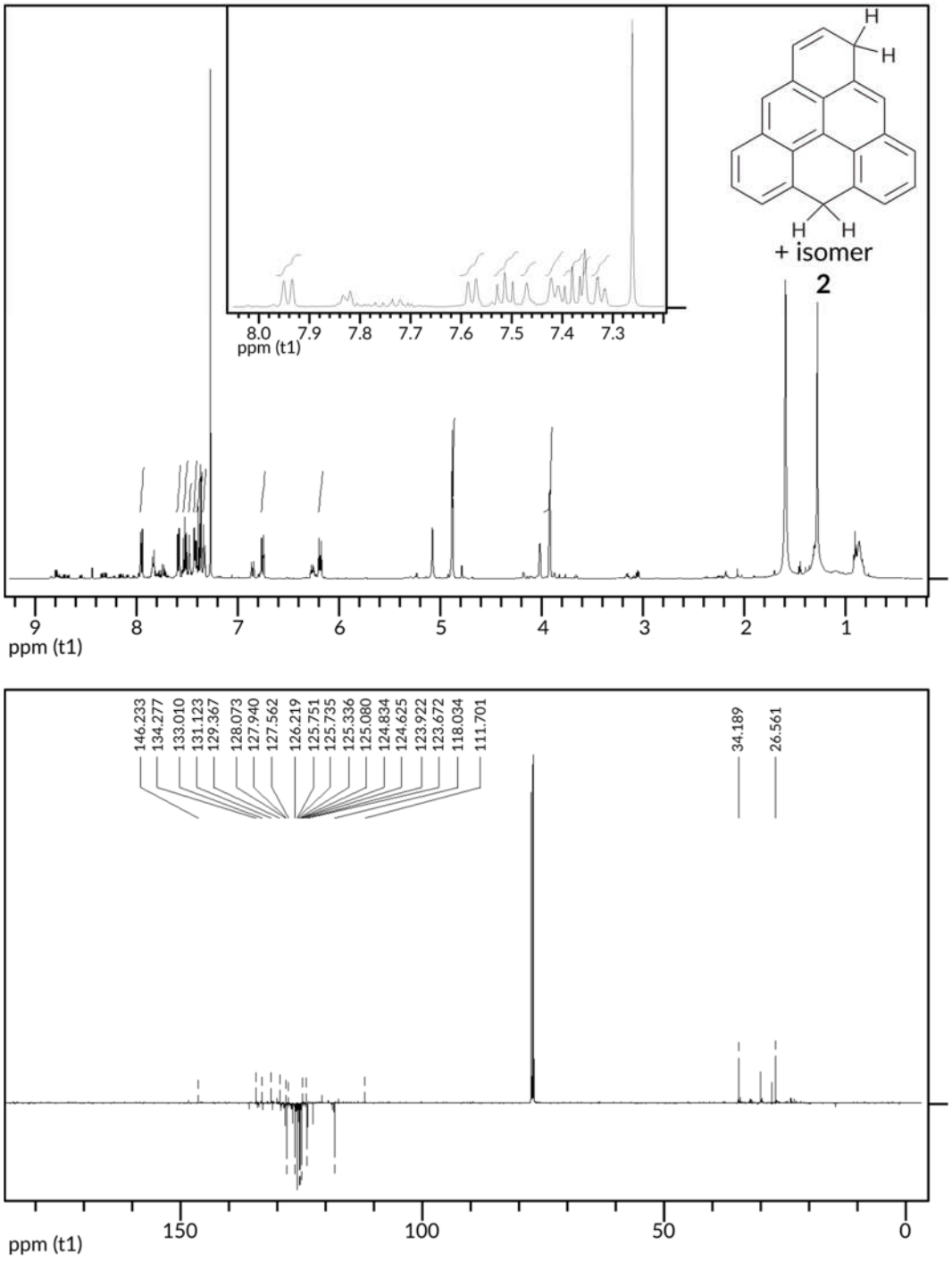

^{1}H (top) and ^{13}C (bottom) NMR spectra of compound **2**.

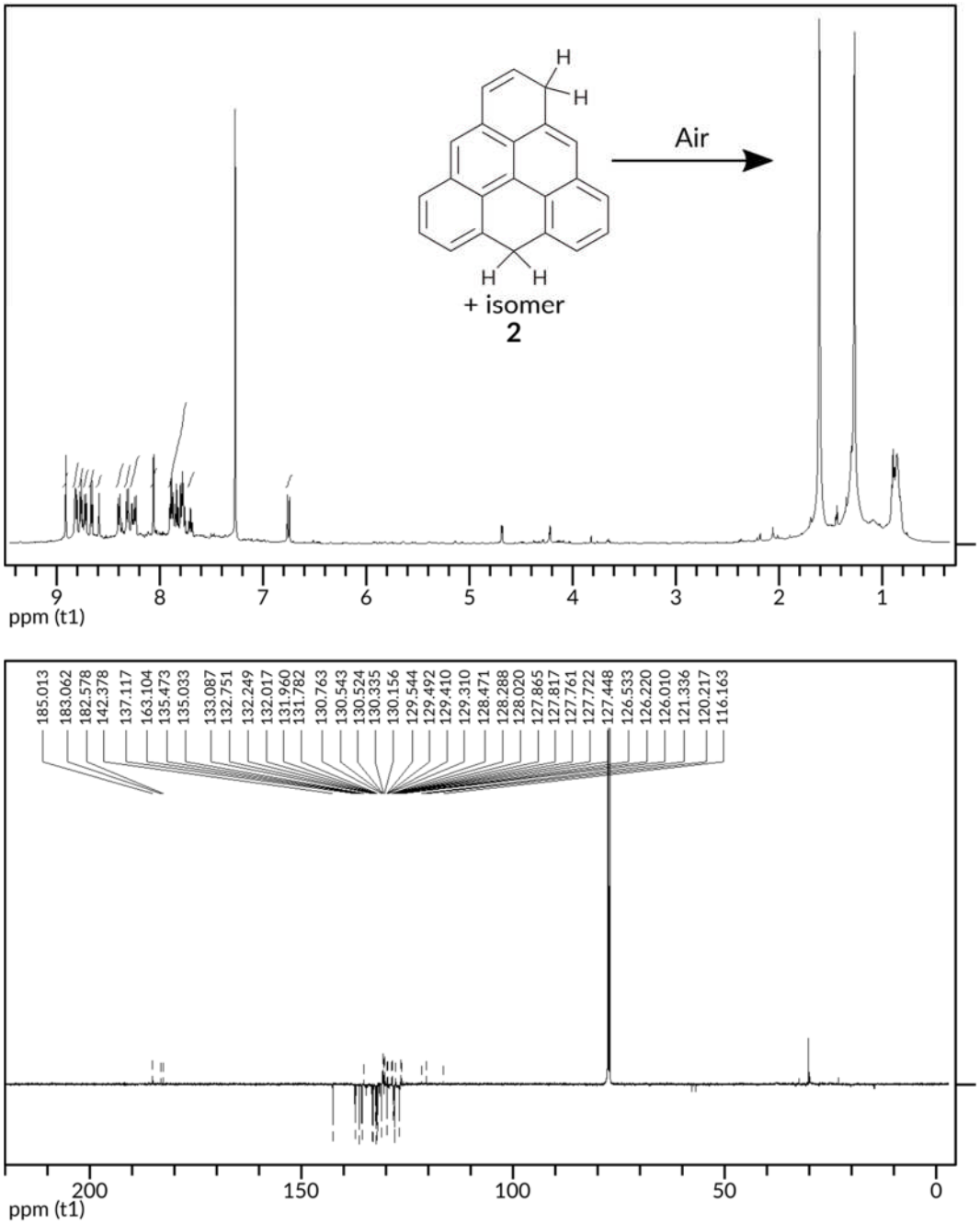

^{1}H (top) and ^{13}C (bottom) NMR spectra of compound **2** after leaving it in a sealed NMR tube in deuterated chloroform. It only took hours to start oxidizing. After 5 days of oxidation two di-ketotriangulene species are observed. However, from the NMR data we cannot conclude which isomers these are.

Supplementary Note 1: Results of DFT-calculations

Dihydrotriangulene isomers

Supplementary Table 1 presents DFT-calculated energies for 11 dihydrotriangulene isomers ($C_{22}H_{14}$, **2a-k** in Supplementary Fig. 2). All isomers differ solely in the location of the hydrogen atoms, whereas the number of carbon (22) and hydrogen (14) atoms is constant with 146 electrons in the system. Hence, their energies can be readily compared with each other. We performed calculations for all possible isomers with CH_2 groups (i.e. additional hydrogens at the outer carbons, **2a-g,i**). In addition, we considered species with out-of-plane hydrogens at inner carbon atoms (**2h,j,k**).

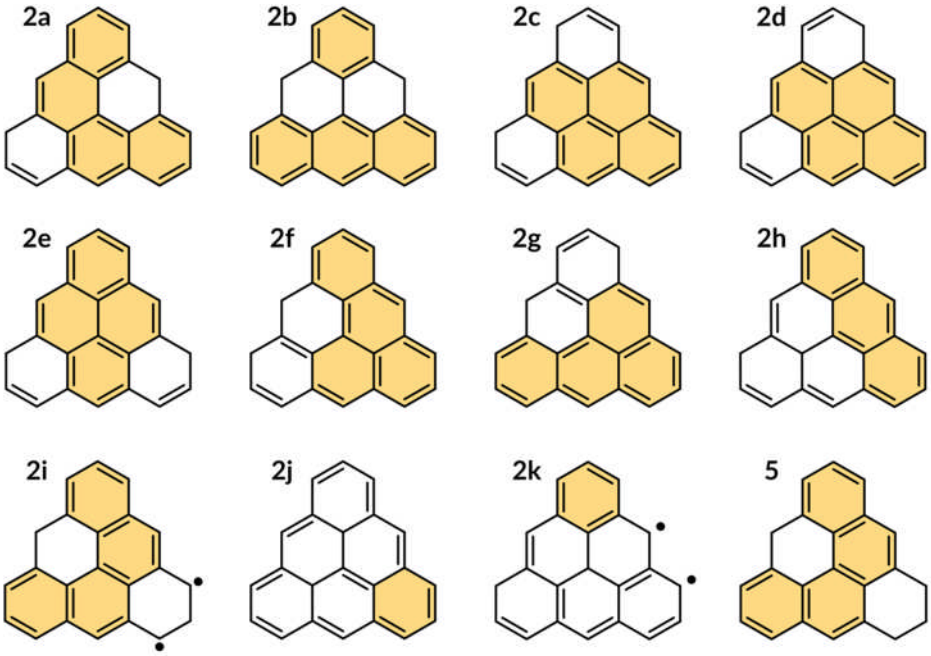

Supplementary Fig. 2: Scheme showing all dihydrotriangulene isomers considered, and the tetrahydro-triangulene isomer **5** ($C_{22}H_{16}$) for reference. Aromatic cores are highlighted orange.

The data shows that isomer **2a** is energetically most favourable, while **2b** is slightly higher in energy by 21 meV. As discussed in the main text isomers with an aromatic pyrene core (**2c** to **2e**) are higher in energy by 207 meV to 305 meV. Other isomers pay significantly higher penalties like, for example, structures **2f** and **2g** comprising an aromatic benzo[*de*]anthracene core (0.631 eV and 0.744 eV higher in energy, respectively).

Furthermore, we calculated structures **2h** and **2j**, isomers with one and two out-of-plane hydrogens, respectively. The non-Kekulé structure **2i** has a CH_2 group at one of the vertices and was mentioned in section 2.2. Only non-Kekulé structures exist for out-of- plane hydrogens at the central carbon atom. Exemplarily, we show structure **2k** with the highest energy in Supplementary Table 1.

Supplementary Table 1: Total DFT energies for all dihydro-triangulene isomers considered. A checkmark (cross) in the third column means that this isomer was (not) observed during STM/AFM measurements of approximately 60 examined individual molecules in total. Energies are given relative to the energy of a **2a** isomer (-23039.096 eV).

Structure	Energy (eV)	Measured	Aromatic core
2a	0	✓	Benzo[*c*]phenanthrene
2b	0.021	✓	Anthracene and benzene
2c	0.207	✗	Pyrene
2d	0.255	✗	Pyrene
2e	0.305	✗	Pyrene
2f	0.631	✗	Benzo[*de*]anthracene
2g	0.744	✗	Benzo[*de*]anthracene
2h	1.133	✗	Anthracene
2i	1.613	✗	
2j	2.446	✗	
2k	2.612	✗	

Magnetic state of triangulene

For free triangulene, the triplet ground state is 349 meV and 165 meV lower in energy than the closed-shell and open-shell singlet states, respectively. This sequence of states is consistent with recent state-of-the-art calculations[52,53].

The energy difference between triplet and singlet reduces marginally for triangulene adsorbed on a layer of Xe on Cu(111) preferring the triplet state by 333 meV over the closed-shell singlet state. This result shows the efficient decoupling of a single layer of Xe, and confirms that triangulene is indeed in its triplet ground state. The decoupling of a single layer of Xe is also substantiated by an adsorption energy of only 0.8 eV, as compared to 2.8 eV for olympicene ($C_{19}H_{12}$) physisorbed on Cu(111)[54]. The adsorption energy was calculated by subtracting the energies of the slab (Cu and Xe) and the free triangulene molecule from the energy of the combined system (Cu, Xe, and adsorbed triangulene molecule).

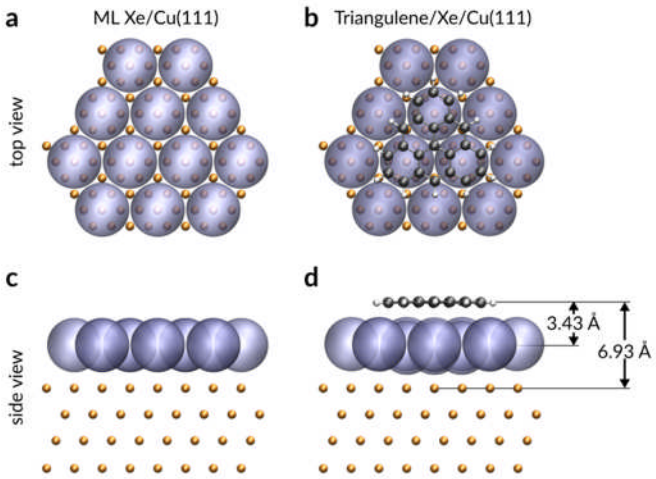

Supplementary Fig. 3: Details of DFT calculations of triangulene adsorbed on 1 ML Xe/Cu(111). **a,b,** (**c,d,**) show renderings for the top (side) views of the relaxed slab and the combined system, respectively. The vertical distances of triangulene with respect to the Xe layer and the topmost Cu layer are indicated in panel **d**.

Supplementary Fig. 3d shows that the equilibrium distance of the molecular plane to the topmost layer of Cu is 6.93 Å. Another way to prove the efficient decoupling of the Xe layer is the PDOS plot for triangulene adsorbed on Xe, presented in Supplementary Fig. 4d that clearly proves that the carbon- and hydrogen-related states are unaffected by the copper- (and xenon-) related states.

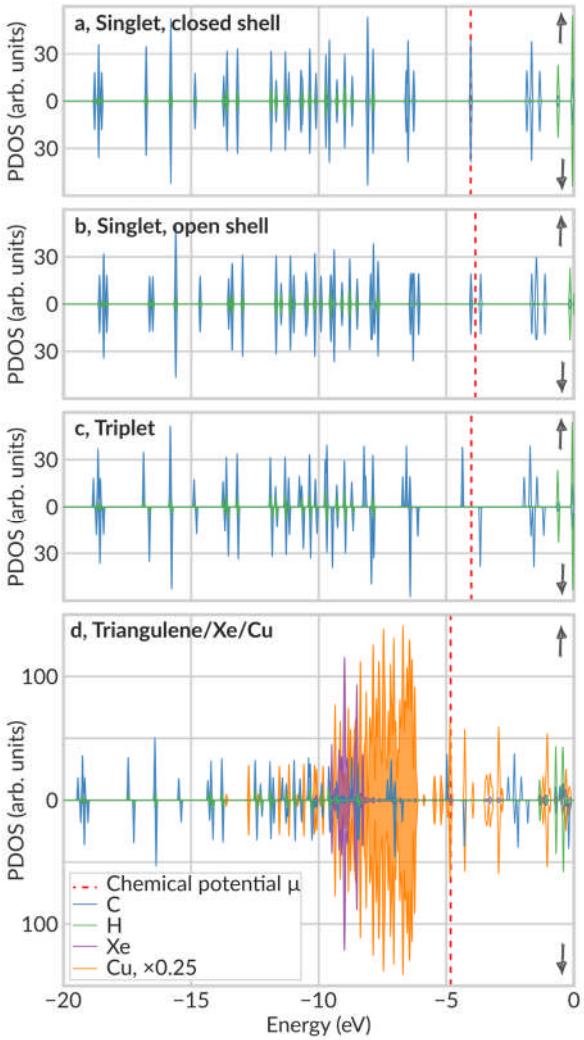

Supplementary Fig. 4: Species-dependent projected density of states (PDOS) plots (at the Γ point of the Brillouin zone) for (**a-c**) the free molecule in the three possible magnetic states and (**d**) triangulene adsorbed on 1 ML Xe on Cu(111). The spin up (down) channels are plotted at the top (bottom) of each panel.

Observed gap in STS

The observed gap in STS between the PIR and the NIR of triangulene is 3.25 eV. This value can be compared to DFT calculations of the free molecule including many-body corrections in the G_0W_0 approximation. The resulting quasiparticle gap (between the pair of occupied levels and the pair of unoccupied levels) is 3.78 eV. We attribute the difference between the calculated gap and the experimentally observed gap to screening from substrate electrons[55, 56].

Supplementary Note 2: Comparison of AFM data to simulated AFM images

Supplementary Fig. 5 shows additional experimental data and includes DFT-calculated charge density maps for all isomers reported in the main text[57]. The charge density maps plotted in Supplementary Fig. 5 correspond to slices of the total electron density of each structure at a height z = 105 pm, where z is defined as the vertical distance to the central carbon atom of the triangulene core. All maps are drawn with the same colour scale. In addition, we show simulated AFM images using the numerical model by P. Hapala *et al.*[58] considering the relaxation of a probe particle (in our case, a CO molecule) due to the tip-molecule interaction. The model is based on empirical Lennard-Jones potentials. The Lennard-Jones parameters are the same that were used in recent literature[59]. The atomic positions were taken from the DFT-calculated geometries. The lateral stiffness of the CO molecule was set to 0.29 N/m, a value that was determined independently for similarly sized molecules[16,17].

For the purpose of structure identification, the experimental and simulated AFM images agree well. However, the model underestimates the distortions that arise because of side groups sticking out from the molecular plane. In line with this observation, the sharpening of the bonds is also underestimated in the model. We rationalize these discrepancies by the fact that, experimentally, the stiffness of the CO molecule at the tip apex is not constant. Rather, the stiffness depends on the tip-molecule interaction and hence will depend on both the lateral and the vertical position of the tip[60].

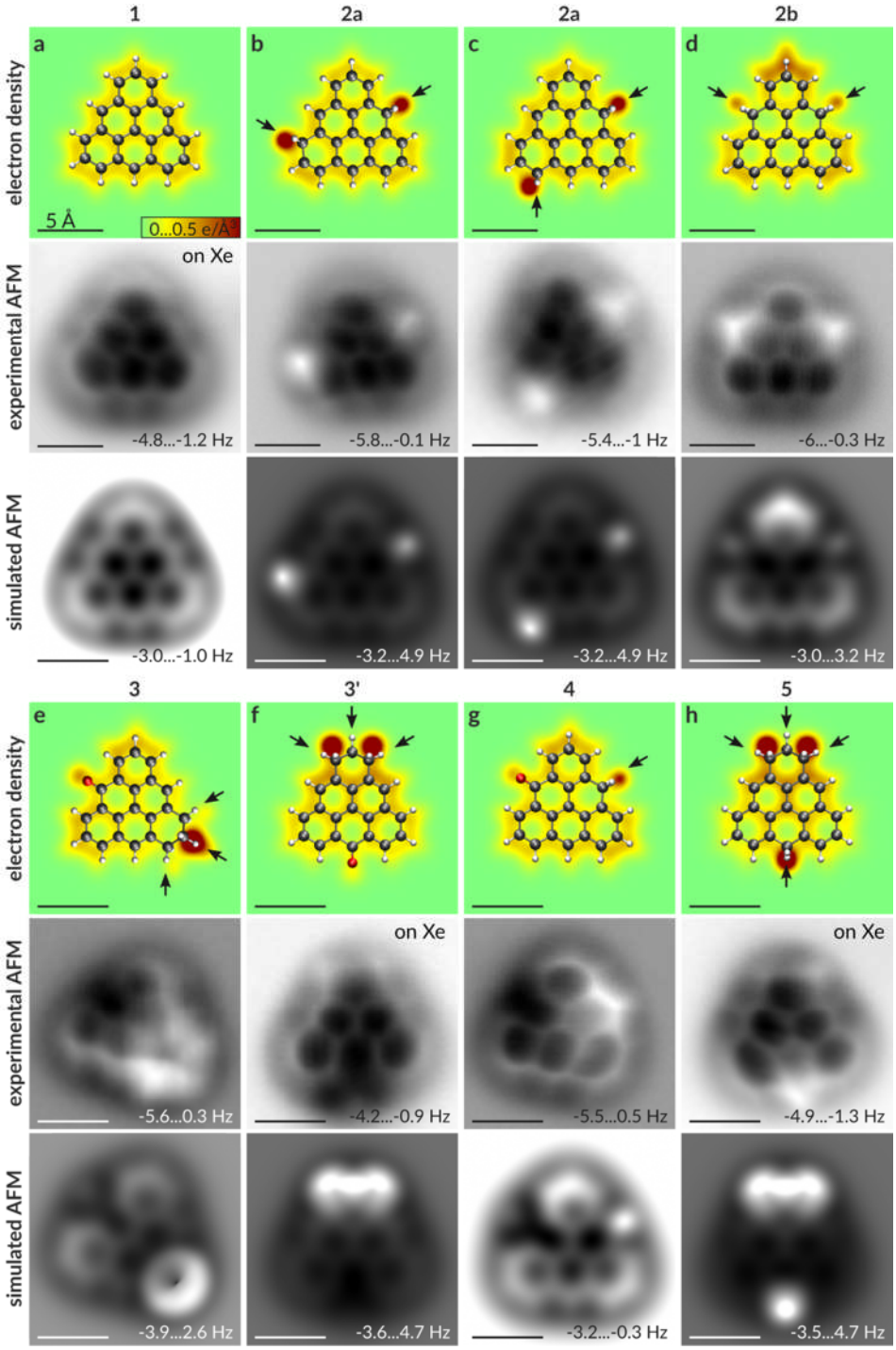

Supplementary Fig. 5: Comparison of AFM data with DFT-calculated charge densities and simulated AFM images. Top rows show electron density maps with molecular models overlaid as a guide to the eye. Arrows indicate positions of CH_2 groups. Middle rows show corresponding AFM data recorded on NaCl (panels **b-e** and **g**) or on Xe (**a, f** and **h**). Bottom rows show simulated AFM images. Note that the AFM data in panels **b**, **d**, **e**, and **g** were already shown in Fig. 2 of the main text. Scale bars, 5 Å.

Note that the charge density of the bonds in the topmost ring of the **2b** isomer shown in Supplementary Fig. 5d is greater than that for the three rings at the bottom of the same image. This is consistent with a fixed Clar sextet in the topmost ring and another, but

migrating, Clar sextet for the anthracene unit. Judging from the AFM data alone, Supplementary Fig. 5e, which we assign as **3** ($C_{22}H_{14}O$), could also be compatible with the non-Kekulé structure **2i** ($C_{22}H_{14}$, see Supplementary Fig. 2). However, there are several arguments against the latter interpretation. For one, we have frequently observed this species, but such a structure is energetically unfavourable. Another argument is based on its non-planar geometry due to three neighbouring CH_2 groups in isomer **3**: we prevalently observed the molecule adsorbed with the two outer hydrogens pointing out of the surface and the central one pointing down on xenon (see Supplementary Fig. 5f; this configuration is denoted as **3'**).

Supplementary Note 3: Comparison of STM orbital images to simulated STM images

Supplementary Fig. 6a compares the energy level scheme of the triplet state (reproduced from Fig. 3c of the main text) to the singlet state. As discussed in the methods section, the singlet state can be modelled either by means of a spin-polarised calculation with the multiplicity restricted to one or by means of a non-polarised calculation. It is clear from the level schemes that both methods give the same result. In the singlet state, levels ψ_2 and ψ_3, which are spin-split in the triplet state, are degenerate and half-occupied. It is clear from their energetic position that the triplet state is favourable for triangulene.

The corresponding single-particle wave functions of the triplet, the open-shell singlet, and the non-polarized calculation equivalent to the closed-shell singlet are shown in Supplementary Figs. 6, b to d, respectively. First, it is obvious that the electron wave functions do not depend on the magnetic state. Second, neither the fully occupied level $\psi_1 \uparrow\downarrow$ nor the fully unoccupied level $\psi_4 \uparrow\downarrow$ match the STM orbital images of triangulene, whereas the superposition of the two pairs of non-disjoint, degenerate orbitals $|\psi_2 \uparrow|^2 + |\psi_3 \uparrow|^2$, shown in Supplementary Fig. 7a, match the STM data.

However, several lobes of the density plot are not resolved in the STM experiments. This can be explained as follows. Commonly, a point-like tip orbital is assumed for interpretation of STM images[36], but in fact the (metallic) tip exhibits an extended *s*-wave leading to a blurring of orbital images[18]. To account for this, we simulated STM images by computing the absolute square of the convolution of an explicit tip wave function and the two degenerate molecular wave functions ψ_2 and ψ_3. For symmetry reasons, calculating the overlap integral of two wave functions as a function of their relative displacement is equivalent to performing a convolution operation[31]. For the tip, we use a generic *s*-wave function ψ_S. Then, we convolve ψ_2 and ψ_3, respectively, with ψ_S. Finally, the absolute squares of the two resulting convolutions are summed up.

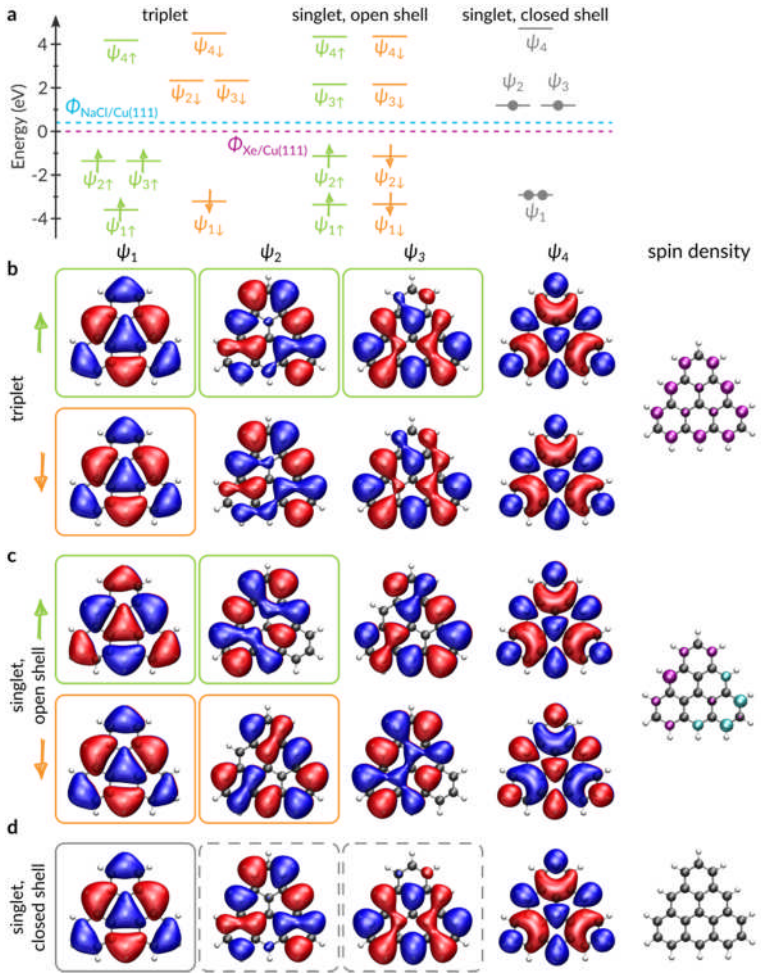

Supplementary Fig. 6: **a,** The same energy level scheme of the (ferromagnetic) triplet state shown in Fig. 3c is compared to similar plots of the (antiferromagnetic) open-shell singlet state in a spin-polarized calculation and (nonmagnetic) closed-shell a spin-restricted (unpolarised) calculation. In case of the triplet, $\psi_{2\uparrow(\downarrow)}$ and $\psi_{3\uparrow(\downarrow)}$ are occupied (unoccupied) in the spin-up (spin-down). In case of the open-shell singlet $\psi_{2\uparrow/\downarrow}$ is occupied and $\psi_{3\uparrow/\downarrow}$ is unoccupied. For the closed-shell singlet (and the equivalent unpolarised), both spin channels are degenerate and ψ_2 and ψ_3 are half-occupied. **b-d,** Plots of the wave functions ψ_1, ψ_2, ψ_3, ψ_4, and the respective spin density for each calculation. The spin-up (spin-down) orbitals are shown in the top (bottom) row of panels **b** and **c**. Solid (dashed) rectangles denote fully (half) occupied levels.

Supplementary Figs. 7, d to f, show contours of constant value of this quantity at three different isovalues. These should therefore approximate experimental STM images at three different tunnelling currents. As observed in the STM experiments, several nodal planes are hidden by the outer lobes at the vertices, and the apparent size of the molecule increases.

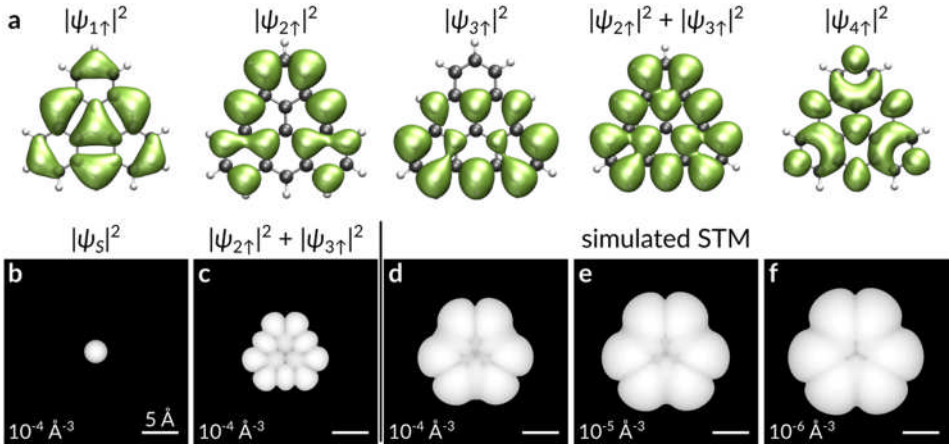

Supplementary Fig. 7: **a,** Contours of constant probability density of triangulene's DFT-calculated frontier molecular orbitals and the superposition of ψ_2 and ψ_3. **b,c,** Probability plots of the *s*-like wave function ψ_S used for the simulated STM images and the superposition of the degenerate molecular orbitals ψ_2 and ψ_3, respectively. **d-f,** Simulated STM images at three different isovalues indicated at the bottom of each panel.

Note that we critically verified that the extent of the *s*-wave (plotted in Supplementary Fig. 7b) is rather underestimated by comparing simulated STM images (using the same parameters) of pentacene's frontier molecular orbitals to experimental images[18].

Supplementary Note 4: STM and AFM data of triangulene on NaCl

Supplementary Figs. 8, a and c, present 1H-triangulene, formed by removal of a hydrogen at position 6 from the **2a** species presented in the main text (Fig. 2e) on the NaCl surface, that is, bilayer NaCl on Cu(111). A subsequent manipulation step to remove one more hydrogen atom led to the structure in the STM image in Supplementary Fig. 8b with the molecule appearing four-fold symmetric.

At first glance, this observation seems puzzling because a C_4-symmetric molecular species is unexpected. However, we show below that a superposition of four equivalent adsorption geometries is measured.

The four-fold symmetry is also apparent in the AFM data in Supplementary Fig. 8d. Supplementary Fig. 8e shows its curvature to highlight the four distinct regions. We can explain the images if in each of the quadrants measured, the molecule is in a different adsorption site. The adsorption site can be obtained by atomically resolved STM data (Supplementary Fig. 8g). The four quadrants are indicated by the dashed lines in Supplementary Fig. 8e that correspond to mirror axes of the underlying NaCl surface with a Na^+ site at the crossing point. Taking advantage of this knowledge, a cropped molecular model of triangulene can be superimposed to match the AFM data in each of the quadrants. The position of the molecule, when the tip is in the right-hand-side quadrant, is shown in Supplementary Fig. 8h. If the tip moves to another quadrant, the molecule rotates into that quadrant accordingly. This interpretation is also supported by features in the damping signal of the AFM sensor (Supplementary Fig. 8f) recorded simultaneously with the AFM data. The bright features are a fingerprint of frequent changes of the molecules' azimuthal orientation. Accordingly, they appear (i) at the borders of two quadrants and (ii) when the tip is approaching the molecule from far away triggering rotations due to the tip-molecule interaction. At positions where dissipation is observed, the molecule presumably changes its adsorption site as a function of tip height during the cantilever's oscillation, with a hysteresis giving rise to dissipation. The effect can be compared to the similar molecular rotations described by Pawlak and co-workers[61].

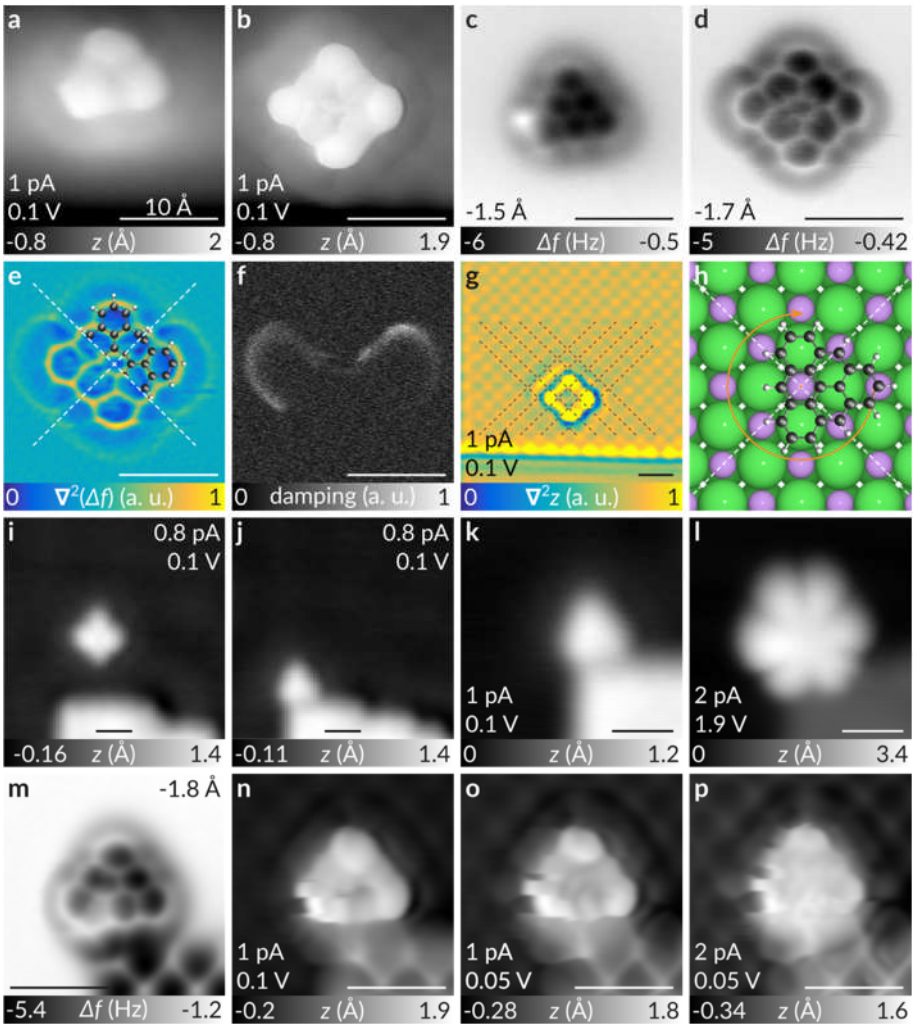

Supplementary Fig. 8: STM and AFM of triangulene generation on NaCl. **a,b,** STM images (CO tip) of molecule shown in Fig. 2e after the first and second manipulation step, respectively. **c,d,** Corresponding AFM images. **e,** Laplace-filtered version of panel **d**. Dashed lines indicate mirror axes of the underlying NaCl surface, and separate the four quadrants of different molecular adsorption sites. Partially cropped structures of triangulene are overlaid as a guide to the eye in two quadrants. **f,** Damping signal of the AFM sensor recorded simultaneously with **d**. High values correspond to higher excitation energy. **g,** Laplace-filtered STM image (CO tip) to determine adsorption site and orientation. Dashed grid lines connecting the Cl sites are partially superimposed. **h,** Rendered model of adsorption geometry, if the tip is in the right-hand-side quadrant of the image. **i-l**, STM images of a triangulene molecule acquired with a metal tip. Panels **i** and **j** were recorded before and after lateral manipulation to a step edge of a three-layer-thick NaCl island, respectively. **k,l,** Zoomed-in images of the same molecule at low voltage and at the NIR, respectively. **m,** AFM image of molecule fixed at step edge to NaCl(3 ML). **n-p,** STM images (CO tip) of the same molecule at different set points.

Note that the C_3 rotational symmetry of triangulene does not match the C_4 symmetry of the underlying NaCl surface. It is possible to break the four-fold symmetry of the substrate using lateral manipulation[24] to move such molecules to a step edge of a three-monolayer-thick NaCl island. This is illustrated by the STM images in Supplementary Figs. 8, i and j, in

which the appearance of the molecule changes from fourfold- to threefold-symmetric, that is, the step edge efficiently blocks full rotations.

However, high-resolution images reveal that adsorption at the step edge is not entirely stable. Supplementary Fig. 8m is an AFM image of the triangulene molecule fixed at the step edge. While the top and the right part of the molecular structure appear sharp and clear, the lower left hexagon is noisy and appears strongly enlarged. We attribute this to small-angle rotations when the tip is positioned above this region. This phenomenon can also be seen in the STM images in Supplementary Figs. 8n-p. The rate of abrupt changes in the topography increases with decreasing tip height, i.e., with increasing tip-molecule interaction. Thus, our data indicate that the rate of small-angle rotations increases with decreasing tip-molecule distance.

In conclusion, we have proved that the potential energy landscape of triangulene adsorbed on NaCl(100) is flat enough to easily overcome the barrier for rotations (25), even though molecules are probed at zero voltage in AFM mode. In other words, the azimuthal orientation of the molecule depends on the tip position.

Supplementary Note 5: Generation sequence of triangulene on NaCl

Supplementary Fig. 9 shows a typical series of STM and AFM images illustrating the manipulation procedure of triangulene on NaCl. First, a suitable precursor molecule was characterized by means of CO tip STM and AFM images (Supplementary Fig. 9, a and b). Next, the CO molecule was deposited on the bare NaCl surface by atomic manipulation to re-establish a clean metal tip. Then, after imaging the molecule again with a metal tip in STM mode (see Supplementary Fig. 9c), dehydrogenation was performed at the position indicated in Supplementary Fig. 9c by ramping the voltage to 3.5 V. In this particular case, the maximum current during manipulation was 40 pA. Supplementary Fig. 9d shows a subsequent STM image acquired with a metal tip demonstrating the apparent four-fold symmetry of triangulene on NaCl. Finally, the generated triangulene molecule is characterized by AFM and STM images with a CO tip (Supplementary Figs. 9, e and f).

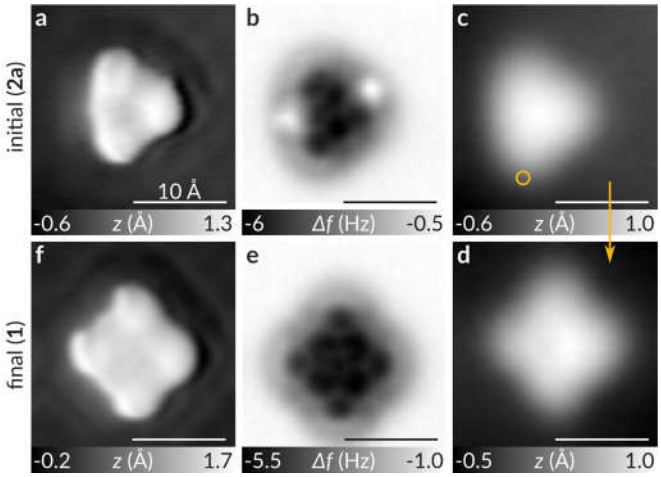

Supplementary Fig. 9: Generation sequence of triangulene generation on NaCl. **a,b,** Initial STM and AFM images (CO tip) of a **2a** molecule on NaCl, respectively. **c,d,** STM images with a metal tip of the same molecule at the same lateral position before and after a voltage pulse had been applied at the position indicated by the orange circle. **e,f,** Final AFM and STM images (CO tip) after successful generation of triangulene, respectively. Imaging conditions: I_{sp} = 0.8 pA, V_{sp} = 0.1 V, Δz = −1.5 Å.

Supplementary Note 6: Charge-state determination of triangulene on NaCl and Xe

Supplementary Fig. 10a shows dI/dV spectra of triangulene on NaCl in comparison to Xe (reproduced from Fig. 3d). On NaCl, the PIR and NIR peaks are centred at -1.8 V and 1.3 V, respectively. As expected from the difference in work functions ($\Phi_{Xe/Cu(111)}$ = 4.4 eV for 1 ML Xe/Cu(111)[29], $\Phi_{NaCl/Cu(111)} \approx$ 4.0 eV for 2 ML NaCl/Cu(111)[30]), both peaks on NaCl are rigidly shifted downwards with respect to the spectrum recorded on Xe.

Scattering of interface state electrons can be employed to deduce the charge state of adsorbates on insulating films[34,35]. The Shockley surface state on Cu(111) survives as an interface state for both substrate system used in this work. Charged adsorbates lead to a standing wave pattern due to scattering of the interface state electrons[34,35]. An example of this effect is presented in Supplementary Figs. 10, b and c, showing different adsorbates (different precursor molecules). Only the adsorbate indicated by a yellow arrow acts as a scattering centre, indicating that it is possibly charged, while no such features are observed for the other four adsorbed molecules seen on this image, proving that they are charge neutral.

Supplementary Figs. 10d-i present STM images of triangulene molecules adsorbed on both NaCl and Xe. None of them exhibits a standing wave pattern confirming the neutral charge state of triangulene on both substrates.

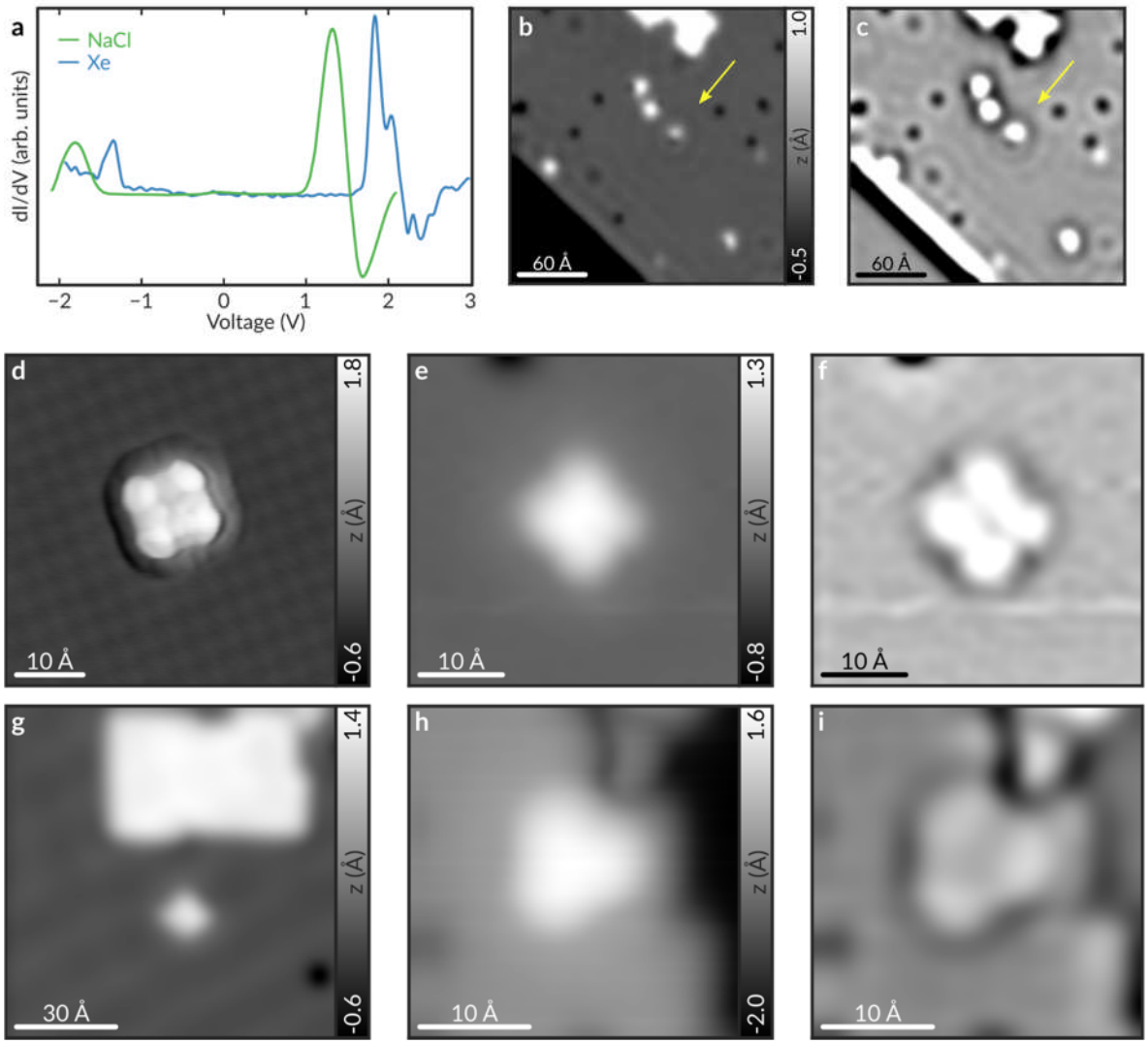

Supplementary Fig. 10: **a**, STS performed at the centre of a triangulene molecule on NaCl (green) and on Xe (blue, reproduced from Fig. 3d). Panels **b** to **i** show STM images at low voltages. **b**, Several precursor molecules on NaCl, out of which only the one marked by a yellow arrow scatters the interface state electrons. **c**, Laplace-filtered version of b. **d-f**, A triangulene molecule on NaCl imaged with a CO tip, a Cu tip, and the Laplace-filtered version of the latter, respectively. **g**, Further example of a triangulene molecule on NaCl. **h,i**, A triangulene molecule on Xe and its Laplace-filtered version, respectively. Note that atomic contrast is observed (in **d**) and standing waves are observed (in **g**), but no scattering at the triangulene molecules can be observed, demonstrating their neutral charge state. Imaging conditions: V = 0.05 V for e-f and V = 0.1 V for all others; I = 2 pA for **i** and I = 1 pA for all others.

Supplementary References

49. Allinson, G., Bushby, R. J., Paillaud, J. L. & Thornton-Pett, M. Synthesis of a derivative of triangulene; the first non-Kekulé polynuclear aromatic. *J. Chem. Soc. Perkin Trans. 1*, 385 (1995).

50. Ye, L. *et al.*, Convenient and versatile synthesis of formyl-substituted benzoxaboroles. *Tetrahedron* **65**, 8738 (2009).

51. Hara, O., Tanaka, K., Yamamoto, K., Nakazawa, T., & Murata, I. The chemistry of phenalenium systems. XXV the triangulenyl dianion. *Tetrahedron Letters* **18**, 2435 (1977).

52. Melle-Franco, M. Uthrene, a radically new molecule? *Chem. Commun.* **51**, 5387 (2015).

53. Das, A., Müller, T., Plasser, F. & Lischka, H. Polyradical Character of Triangular Non-Kekulé Structures, Zethrenes, p-Quinodimethane-Linked Bisphenalenyl, and the Clar Goblet in Comparison: An Extended Multireference Study. *J. Phys. Chem. A* **120**, 1625 (2016).

54. Liu, W. *et al.*, Identical binding energies and work functions for distinct adsorption structures: olympicenes on the Cu(111) surface. *J. Phys. Chem. Lett.* **7**, 1022 (2016).

55. Jiang, X. *et al.*, Giant quasiparticle bandgap modulation in graphene nanoribbons supported on weakly interacting surfaces. *Appl. Phys. Lett.* **103**, 133107 (2013).

56. Ruffieux, P. *et al.*, Electronic structure of atomically precise graphene nanoribbons. *ACS Nano*. **6**, 6930 (2012).

57. Moll, N., Gross, L., Mohn, F., Curioni, A. & Meyer, G. A simple model of molecular imaging with noncontact atomic force microscopy. *New J. Phys.* **14**, 083023 (2012).

58. Hapala, P. *et al.*, Mechanism of high-resolution STM/AFM imaging with functionalized tips. *Phys. Rev. B* **90**, 085421 (2014).

59. Van der Lit, J., Di Cicco, F., Hapala, P., Jelínek, P. & Swart, I. Submolecular resolution imaging of molecules by atomic force microscopy: the influence of the electrostatic force. *Phys. Rev. Lett.* **116**, 096102 (2016).

60. Neu, M. *et al.*, Image correction for atomic force microscopy images with functionalized tips. *Phys. Rev. B* **89**, 205407 (2014).

61. Pawlak, R., Fremy, S., Kawai, S., Glatzel, T., Fang, H., Fendt, L.-A., Diederich, F. & Meyer, E. Directed Rotations of Single Porphyrin Molecules Controlled by Localized Force Spectroscopy. *ACS Nano* **6**, 6318 (2012).